TECHNISCHE UNIVERSITÄT WIEN

INSTITUT FÜR PHOTONIK
Photonics Institute

DIPLOMARBEIT

Dark Transport in Polaritonic Semiconductor Quantum Structures

zur Erlangung des akademischen Grades

Diplom-Ingenieur

im Rahmen des Studiums

Technische Physik

eingereicht von

Elias Plankenbichler
Matrikelnummer 01609371

ausgeführt am Institut für Photonik
der Fakultät für Elektrotechnik und Informationstechnik
der Technischen Universität Wien

Betreuung
Betreuer: Univ.Prof. Mag.rer.nat. Dr.rer.nat. Karl Unterrainer
Mitwirkung: Dr.techn. Benedikt Limbacher

Wien, 18.01.2024

Unterschrift Verfasser

Unterschrift Betreuer

Abstract

In this work, we investigate semiconductor quantum structures in the search of a dark transport of electrons induced by vacuum fluctuations. Recently, many advances have led to a better understanding of the influence of vacuum effects on quantum systems, like the significant enhancement of the conductivity in organic semiconductors [1] or the breakdown of topological protection caused by the cavity vacuum field in the integer quantum hall effect [2]. Theories attempt to explain these effects, emphasizing the importance of the antiresonant terms in the light-matter coupling Hamiltonian [3, 4]. We achieve a strong coupling of electrons to the vacuum electromagnetic field by embedding structures with an inherent intersubband transition of 100 meV in a cavity. We use a nanofabrication process to build micro patch resonators down to a patchsize of 1 µm and accomplish to form a superstructure for contacting single 2 µm resonators electrically. We measure polaritons in a doped Resonant Tunneling Diode structure [5] by Fourier-Transform-Infrared spectroscopy and thereby prove the functionality and tunability of the cavity. We determine the patchsize resonant with the intersubband transition and show that the Rabi splitting is still present in 2 µm resonators. Furthermore, we perform low temperature measurements on the transport using a cryogenic probe station. Our investigations include Multiple Quantum Well structures similar to Quantum Well Infrared Photodetectors, which we optimised to study a vacuum-induced transport. As the basic building blocks of a Quantum Well Infrared Photodetector are well-understood, we utilize it as a tool to gain a deep insight into the coupling of electrons to virtual photons. We consider different patchsizes attempting to tune the vacuum effect strength by the cavity mode volume and include 5 µm resonators which represent the off-resonant case. We measure the transport in the micro patch resonators at a temperature of 4.3 K and show transport anomalies in 2 µm resonators in three different structures, which we explain by an interplay of a dark transport and surface effects.

Kurzfassung

In dieser Arbeit beschäftigen wir uns mit Halbleiter-Quantenstrukturen auf der Suche nach einem durch Vakuumfluktuationen hervorgerufenen dunklen Transport von Elektronen. Forschung zu dem Thema führte in letzter Zeit zu einem besseren Verständnis des Einflusses von Vakuumeffekten auf Quantensysteme, wie zum Beispiel die signifikante Erhöhung der Leitfähigkeit in organischen Halbleitern [1] oder der nachgewiesene Zusammenbruch topologisch geschützter Zustände durch das Cavity-Vakuumfeld im Integer-Quantum-Hall Effekt [2]. Theorien versuchen diese Effekte zu erklären, wobei die Bedeutung der antiresonanten Terme der Licht-Materie Wechselwirkung im Hamiltonian betont wird [3, 4]. Wir erreichen in dieser Arbeit eine starke Kopplung von Elektronen an das elektromagnetische Vakuumfeld, indem wir Strukturen mit einem inhärenten Intersubband-Übergang von 100 meV in eine Cavity einbetten. Mithilfe eines Nanoherstellungsprozesses stellen wir Micro-Patch-Resonatoren bis zu einer Patch-Größe von nur 1 µm her und designen eine Überstruktur um einzelne 2-µm-Resonatoren elektrisch zu kontaktieren. Wir messen Polaritonen in einer dotierten Resonanten Tunneldiodenstruktur [5] mittels Fourier-Transform-Infrarot-Spektroskopie und weisen damit die Funktionalität und Durchstimmbarkeit der Resonatoren nach. Wir bestimmen die Patchgröße, die mit dem Intersubband-Übergang resonant ist und zeigen, dass das Rabi-Splitting in 2-µm-Resonatoren noch vorhanden ist. Außerdem führen wir Tieftemperatur-Strommessungen mit einer Helium-gekühlten Probestation durch. Unsere Untersuchungen umfassen zwei Multi-Quantentopf-Strukturen, ähnlich den sogenannten Quantentopf-Infrarot-Photodetektoren, die wir für die Suche nach einem vakuuminduzierten Strombeitrag optimieren. Da die grundlegenden Bausteine eines Quantentopf-Infrarot-Detektors gut verstanden sind, nutzen wir diesen als Werkzeug, um einen tiefen Einblick in die Wechselwirkung zwischen Elektronen und virtuellen Photonen zu gewinnen. Wir betrachten verschiedene Patch-Größen und versuchen, die Stärke der Vakuumeffekte durch eine Variation des Cavity-Modenvolumens zu beeinflussen. Wir messen den Transport in einzelnen Patch-Resonatoren bis zu einer Patchgröße von nur 2 µm und inkludieren darüberhinaus 5-µm-Resonatoren, die den off-resonanten Fall darstellen. Wir finden eine klare Abhängigkeit der Stromdichte von der Patchgröße vor und zeigen Transportanomalien in 2-µm-Resonatoren in drei verschiedenen Strukturen, welche wir durch ein Zusammenspiel von dunklem Transport und Oberflächeneffekten erklären.

Contents

1 Introduction

People usually connect the term 'vacuum' with empty space, where no particles are present. However, more accurately, in QED the vacuum is defined as the ground state of the quantized electromagnetic field from which no energy can be extracted. Within this theory, the vacuum is not empty but rather filled with virtual particles that are incessantly created and annihilated, which is referred to as vacuum fluctuations. This fascinating property of the vacuum leads to observable effects like the Casimir effect. In 1948, Casimir proved that an attractive force appears between two plane, neutral and perfectly conducting plates which are placed in parallel in the vacuum. Casimirs concept of the vacuum included the idea that the zero-point energy of the vacuum changes whenever it underlies external constraints, which is the case for all interactions with external fields or matter present. These constraints in turn lead to a response of the vacuum state resulting in a force between the plates. With this experiment, a solid basis for the discussion of the vacuum zero-point energy in field theory was formed [6]. Casimir already examined one of the most paradigmatic cases, namely a cavity placed in the vacuum. This configuration leads to clear boundary conditions that must be satisfied by the vacuum electromagnetic field resulting in discrete spatial modes and a reduced mode density in the region between the plates [7]. A further example for the influence of the vacuum field is spontaneous emission. In 1946 Purcell investigated transitions of the nuclear magnetic moment in hydrogen nuclei and showed that the spontaneous emission rate is increased when the atom is embedded in a cavity resonant with the corresponding transition [8]. The rate is determined by the vacuum field mode density and, thus, the presence of the cavity by reducing the mode density increases the rate, if the cavity mode is resonant with the transition. Compared to the free space value, the rate is increased by the ratio of the mode densities of the two cases. Purcell's work marks the beginning of the topic area Cavity QED [9]. However, not only a change of the vacuum mode density due to boundary conditions leads to effects in a physical system but also the emergence of pairs of virtual photons has an impact, resulting in radiation corrections like the Lamb shift. The transition energy of the hydrogen atom is thereby shifted due to virtual interactions, where the main contribution comes from the emission and reabsorption of virtual photons, which was shown already in a nonrelativstic treatment by Bethe [9]. Based on vacuum fluctuations another phenomenon was theoretically predicted in 1970, which is known as dynamical Casimir effect [10].

It describes the creation of real photon pairs out of the vacuum by means of a mirror moving with a speed close to the speed of light. An analogous effect is believed to occur by a non-adiabatic change of certain system properties. Recent experiments have potentially demonstrated such effects [11, 12]. Concluding we know that even though it is not possible to extract energy from the vacuum state, we can investigate physical effects that appear due to the interaction of a given system with vacuum field fluctuations. Thus, by vacuum-field engineering we attempt to optimize the system under investigation to show a certain behavior upon interaction with the vacuum zero-point field. In 2015 the possibility to enhance the conductivity in organic semiconductors by one order of magnitude by utilizing vacuum fluctuations was shown [1]. This transport enhancement through the coupling of electronic states to the vacuum field finds application in the improvement of thin-film-transistors. A further effect discovered recently is the breakdown of topologically protected states in the integer quantum Hall effect. Here, the non-locality of the cavity vacuum field leads to a destruction of the topological order in the system, as electrons are in principal protected from backscattering, but cavity mediated long-range hopping processes influence the electronic states and lead to a finite resistivity [2]. These examples show that vacuum field effects can crucially influence the electronic states in solid state systems, which is also the focus of our work. A powerful method for observing strong light-matter coupling uses so-called intersubband (ISB) transitions in Quantum Well (QW) structures based on semiconductor material systems. The study of intersubband polaritons was first proposed by Liu in 1997, when he made promising theoretical predictions. Subsequently, Dini et. al. were the first to measure the corresponding polariton splitting experimentally in 2003. Since then, ISB transitions were extensively studied as their good tunability and large transition dipole moment in the order of tens of angstroms highlights them as a powerful tool to investigate the electronic and optical properties determined by (ultra-) strong light-matter coupling phenomena [13]. In the well-known light-matter coupling Hamiltonian so-called antiresonant terms occur, which build the energy contribution caused by the coupling to vacuum fluctuations. However, in first order perturbation theory they are irrelevant as the coupling of pairs of virtual photons results in a changed number of excitations in the system and, thus, the matrix element is zero. Nevertheless, in a second order treatment transitions over intermediate states caused by virtual interactions are possible, resulting in a non-zero contribution to the electronic energy caused by the antiresonant terms. Thus, in this work we investigate Multiple Quantum Well (MQW) structures and search for effects on the transport caused by electronic excitations that are created through virtual interactions. In order to maximize the vacuum influence we

couple an ISB transition to the vacuum field by embedding the structure in a cavity and aim for observing a vacuum-induced transport in the dark. Moreover, we attempt to tune the effect by changing the cavity mode volume according to recent theoretical work on the topic [4]. Besides the potential to gather fundamental insights, our work is also relevant for applicative reasons. We build devices based on a Resonant Tunneling Diode (RTD) structure which was shown to maintain its transport behavior in the strong coupling regime, where at the same time a modulation of the coupling strength was accomplished by a variation of the applied voltage [5]. Furthermore, we focus on MQW structures which are similar to so-called Quantum Well Infrared Photodetectors (QWIPs), which are important for spectroscopy and sensing in the mid-IR range and are usually operated in the weak coupling regime. However, the use of strongly coupled detector structures is expected to have significant advantages [14] and, thus, our work contributes to future applications.

2 Theory

In this chapter a brief introduction to the fundamental physics of the investigated samples will be given.

2.1 Quantum Wells

In this work we investigate so-called intersubband (ISB) transitions between two discrete states in quantum wells (QWs), which are formed by the conduction bands of two alternating materials with different bandgap energies. The layers which build the QWs are grown by Molecular Beam Epitaxy (MBE) and have thicknesses in the nanometer range. If an electron is located in such a small region, according to the Heisenberg uncertainty principle its momentum increases

$$\Delta p \geq \frac{\hbar}{\Delta x} \ , \tag{2.1}$$

leading to a finite kinetic energy, even in the ground state. The electron wavefunction is described by the Schrödinger equation

$$-\frac{\hbar^2}{2m_e}\frac{\partial^2}{\partial x^2}\psi(x) + V(x)\psi(x) = E\psi(x) \ , \tag{2.2}$$

which for the QW region, where V = 0, simplifies to

$$-\frac{\hbar^2}{2m_e}\frac{\partial^2}{\partial x^2}\psi(x) = E\psi(x) \ . \tag{2.3}$$

The solution for the free electron case is found by a plane-wave approach

$$\psi(x) = Ae^{ikx} + Be^{-ikx} \ . \tag{2.4}$$

We now account for the QW barriers by applying the boundary conditions

$$\psi(x \leq 0) = \psi(x \geq a) = 0 \tag{2.5}$$

and, hence, we find the stationary electronic states in analogy to standing waves in a vibrating string. The wavefunctions are determined by discrete wavenumbers $k = \frac{n\pi}{a}$ and corresponding eigenenergies

$$E_n = \frac{\hbar^2\pi^2}{2m_e}\frac{n^2}{a^2} \ , \tag{2.6}$$

where n is an integer number $n = 1, 2, ..$ and m_e is the electron mass [15]. Of course in real systems the QWs are formed by potential barriers of finite height and, thus, the wavefunctions to some extent penetrate into the barriers. A sketch of a QW with finite height is shown in figure 2.1. The electron can occupy a number of different states $|\psi_i\rangle$ in the QW, where we switched from a position representation to the more general bra-ket notation. Transitions between the states are possible through photon absorption or emission, providing that the selection rules for electric dipole radiation are met. In this work we are only interested in the ground and first excited states of the QWs $|g\rangle \equiv |\psi_1\rangle$ and $|e\rangle \equiv |\psi_2\rangle$ and the ISB transition between the two. In section 3.1.1 we will present the designed MQW structures, for which the first excited state is already on the edge of the QW and, thus, we do not account for any higher excited states. Moreover, this simplifies the mathematical description as it enables us to treat the QW as a two-level system.

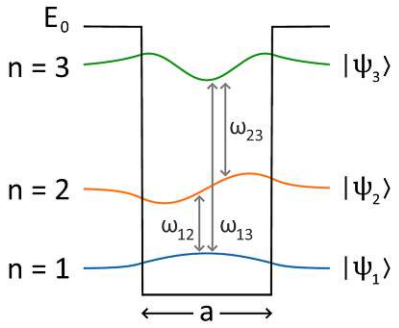

Figure 2.1: Sketch of a quantum well with height E_0 and width a, leading to electronic states with discrete energies. Due to the finite height of the QW, the electron wavefunction penetrates into the barriers, where it decreases exponentially. A transition from an initial state $|\psi_i\rangle$ to a state $|\psi_j\rangle$ is possible by absorption or emission of a photon, whose energy has to match the transition energy $\hbar\omega_{ij}$.

As we will consider structures with multiple QWs separated by barriers with finite width, another relevant phenomenon is electron tunneling. When we consider an electron with kinetic energy E moving towards a potential barrier with width a and height E_0, we find the tunneling probability in 1D [15]

$$T = \frac{1 - \frac{E}{E_0}}{(1 - \frac{E}{E_0}) + (\frac{E_0}{4E}) \cdot sinh^2(\alpha a)} \tag{2.7}$$

where $\alpha = \frac{\sqrt{2m_e(E_0 - E)}}{\hbar}$. For systems where E and E_0 are fixed, the probability only depends on the width of the barrier a and, thus, can be tuned by it. MQW structures are

also used in so-called Quantum Well Infrared Photodetectors (QWIPs). When light hits such a device at a normal angle of incidence, there is no electric field component in Z-direction, which is needed for the ISB transition. To conquer this, these detectors use e.g. diffraction gratings to obtain a Z-component of the electric field and fulfill the transition rules, which leads to an enhanced absorption efficiency. However, these structures are not optimized to increase the coupling strength. Therefore, in this work we choose a different approach and embed the structure in a microcavity. Light which is resonant with the cavity, then, couples strongly to the structure, where the corresponding mode implies a finite field component in Z-direction. For a cavity resonant with the ISB transition, so-called polaritons appear in the system due to a hybridization of the cavity mode with the electronic transition.

2.2 Polaritons

Let us consider a Hamiltonian which describes a system with two substates and corresponding eigenenergies E_1 and E_2 which do not interact with each other. The Hamiltonian in diagonal form then reads

$$H = \begin{pmatrix} E_1 & 0 \\ 0 & E_2 \end{pmatrix} \quad . \tag{2.8}$$

When we now apply a pertubation of the Form

$$V = \begin{pmatrix} 0 & W \\ W^* & 0 \end{pmatrix} \quad , \tag{2.9}$$

the Hamiltonian of the perturbed system is of the form

$$H' = H + V = \begin{pmatrix} E_1 & W \\ W^* & E_2 \end{pmatrix} \quad . \tag{2.10}$$

We now calculate the eigenenergies of the perturbed Hamiltonian and obtain

$$E_\pm = \frac{1}{2}(E_1 + E_2) \pm \frac{1}{2}\sqrt{(E_1 - E_2)^2 + 4|W|^2} \quad . \tag{2.11}$$

For two states which are initially degenerate $E_1 = E_2 = E_0$, the new eigenenergies become

$$E_\pm = E_0 \pm |W| \quad . \tag{2.12}$$

In Figures 2.2a and 2.2b the energies of the two substates are shown for the unperturbed and perturbed case. By tuning $E_1 = E_2 + \Delta E$ in a system described by H, the energies are crossing at $\Delta E = 0$. In contrast, for a system described by H' the crossing is avoided.

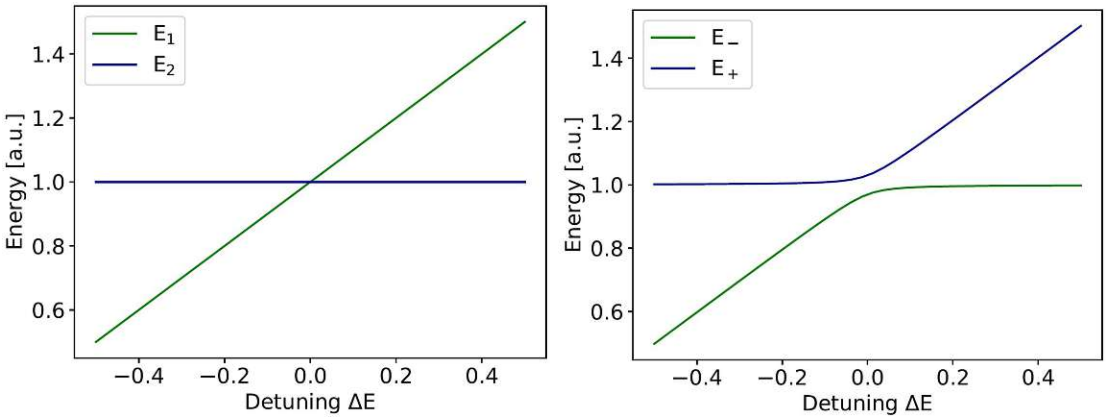

Figure 2.2: Energies E_1 and E_2 of two substates, where $E_1 = E_2 + \Delta E$ is tuned through and E_2 is constant. (a) Without interaction, the energies of the two substates cross at zero detuning. (b) In the perturbed system, the energies split up by $2|W|$ to avoid degeneracy.

The new system states are superpositions of the initial states and the degenerate energy levels split up by $2|W|$. This very general behavior can be retrieved in the system we investigate in this work. We consider now an ISB transition which is embedded in a cavity and start with the well-known dipole coupling Hamiltonian [7]

$$H = \hbar\omega_{12} |e\rangle \langle e| + \sum_k \hbar\omega_k a_k^\dagger a_k - \vec{d} \cdot \vec{E}(\vec{x}) \tag{2.13}$$

where we chose the zero point of energy to be at the QW ground state. The first term describes the ISB transition, the second term accounts for the photons in the cavity and the last term describes the interaction between the two. For a fundamental cavity mode in resonance with the ISB transition, it is justified to consider only a single bosonic mode k_0, since in this case the mode spacing is of the order of the mode energy. Thus, by neglecting higher order modes we find the Jaynes-Cummings Hamiltonian

$$H = \hbar\omega_{12} |e\rangle \langle e| + \hbar\omega_c a^\dagger a - \vec{d} \cdot \vec{E}(\vec{x}) \tag{2.14}$$

with $a = a_{k_0}$, $\omega_c = k_0 c$. Let us now consider the quantized electric field contributing to the interaction term in the Hamiltonian. For a Fabry-Perot cavity built by two mirrors facing each other which are separated by a distance L along the X-axis, the possible modes are characterized by $k = \frac{n\pi}{L}$. For a single mode k_0, the electric field operator reads [16]

$$\vec{E}(\vec{x}) = -i\vec{\epsilon}\sqrt{\frac{\hbar\omega_c}{\epsilon_0 V}} sin(k_0 x)(a - a^\dagger) \ . \tag{2.15}$$

where V is the mode volume $V = A \cdot L$ and $\vec{\epsilon}$ is the normalized polarisation operator $|\vec{\epsilon}| = 1$ which is perpendicular to $\vec{k}$ resulting in two possible polarisation directions. With the quantized electric field we already implied a second quantization formalism, which we exploit even further by considering the photon number states $|n\rangle$ which are eigenstates of H_{EM}. The so-called occupation number operator $\hat{n} = a^\dagger a$ has eigenvalues n corresponding to the number of photons in the cavity

$$\hbar\omega_c a^\dagger a \,|n\rangle = n\hbar\omega_c \,|n\rangle \tag{2.16}$$

with the eigenenergies

$$E_n = n\hbar\omega_c \ . \tag{2.17}$$

In this basis, we find that the mean electric field vanishes [7]

$$\langle n|\, \vec{E}\, |n\rangle = 0 \ , \tag{2.18}$$

whereas at the same time the electric field fluctuations are finite

$$\langle n|\, E^2\, |n\rangle = \sqrt{\frac{\hbar\omega_c}{\epsilon_0 V}}(2n+1) \ . \tag{2.19}$$

In fact, this is true even if the system is in the vacuum state, or in other words, in the absence of photons in the cavity

$$\langle 0|\, E^2\, |0\rangle = \sqrt{\frac{\hbar\omega_c}{\epsilon_0 V}} \ . \tag{2.20}$$

These so-called vacuum fluctuations build the core of our investigations. We now consider only states of the system which correspond to a single excitation, i.e. either a ground state electron and a cavity photon or an excited state electron with no photons in the cavity

$$\{|g,1\rangle, |e,0\rangle\} \ . \tag{2.21}$$

In this basis, the Hamiltonian in 2.14 without the interaction term becomes

$$H = \begin{pmatrix} \hbar\omega_c & 0 \\ 0 & \hbar\omega_{12} \end{pmatrix} \ . \tag{2.22}$$

The interaction Hamiltonian reads

$$H_{int} = -\vec{d}\cdot\vec{E}(\vec{x}) \ , \tag{2.23}$$

where the dipole operator is given by

$$\vec{d} = \vec{d}_{eg}\,|e\rangle\langle g| + \vec{d}^*_{eg}\,|g\rangle\langle e| \tag{2.24}$$

with the transition dipole moment $\vec{d}_{eg} = \langle e|\,\vec{d}\,|g\rangle$. In the case of an ISB transition where the growth direction is in Z-direction, $\vec{d}_{eg}$ is also oriented along the Z-direction $\vec{d}_{eg} = d_{eg} \cdot \vec{e_z}$. It immediately follows the polarisation selection rule that the electric field must have a non-zero component in Z-direction to enable a transition $\vec{\epsilon} \cdot \vec{e}_z \neq 0$. We now introduce the so-called jump operators

$$\begin{aligned} \sigma_+ &= |e\rangle\langle g| \\ \sigma_- &= |g\rangle\langle e| \end{aligned} \tag{2.25}$$

and write the dipole operator in the form

$$\vec{d} = \vec{d}_{eg}(\sigma_+ + \sigma_-) \tag{2.26}$$

where for simplicity we assumed $\vec{d}_{eg} = \vec{d}^*_{eg}$. With the expression for the electric field in 2.15 we now find the new form of the interaction Hamiltonian

$$H_{int} = i\,\vec{d}_{eg}\sqrt{\frac{\hbar\omega_c}{\epsilon_0 V}}\,\vec{\epsilon}\,sin(k_0 x)\,(\sigma_+ + \sigma_-)(a - a^\dagger) \ . \tag{2.27}$$

We now perform a unitary transformation $a \mapsto ae^{i\phi}$, where $\phi = \frac{\pi}{2}$, to absorb the minus sign of $a^\dagger$ in the interaction Hamiltonian and define the so-called Rabi frequency

$$\Omega := \frac{\vec{d}_{eg} \cdot \vec{E}_0}{\hbar} \tag{2.28}$$

with

$$\vec{E}_0 = -\sqrt{\frac{\hbar\omega_c}{\epsilon_0 V}}\,\vec{\epsilon}\,sin(k_0 x) \ . \tag{2.29}$$

We can now write

$$H_{int} = \hbar\Omega(\sigma_+ a + \sigma_- a^\dagger + \sigma_+ a^\dagger + \sigma_- a) \tag{2.30}$$

and, thus, the full Hamiltonian becomes

$$\begin{aligned} H = \hbar\omega_{12}\sigma_+\sigma_- + \hbar\omega_c a^\dagger a \\ + \hbar\Omega(\sigma_+ a + \sigma_- a^\dagger + \sigma_+ a^\dagger + \sigma_- a) \ . \end{aligned} \tag{2.31}$$

The first two terms of H_{int} are called resonant terms, whereas the last two terms are referred to as antiresonant terms. The antiresonant terms correspond to the coupling to vacuum fluctuations and are usually neglected in the so-called Rotating Wave Approximation (RWA). Within the RWA we obtain the matrix representation of the Hamiltonian

$$H = \begin{pmatrix} \hbar\omega_c & \hbar\Omega \\ \hbar\Omega & \hbar\omega_{12} \end{pmatrix} \tag{2.32}$$

with the corresponding energy eigenvalues

$$\begin{aligned} E_{\pm} &= \frac{\hbar}{2}(\omega_c + \omega_{12}) \pm \frac{\hbar}{2}\sqrt{(\omega_c - \omega_{12})^2 + 4\Omega^2} \\ &= \hbar\omega_c - \frac{\hbar}{2}\Delta \pm \frac{\hbar}{2}\sqrt{\Delta^2 + 4\Omega^2} \quad , \end{aligned} \tag{2.33}$$

where in the last line we introduced the detuning $\Delta := \omega_c - \omega_{12}$. For small detuning, the two energies are actually the energies of the upper and lower polariton. A polariton is a quasiparticle formed by the superposition of an electron with a photon. This gets more clear if we look at the new system states, for which the Hamiltonian becomes diagonal

$$\begin{aligned} |UP\rangle &= \frac{1}{\sqrt{2}}(|g,1\rangle + |e,0\rangle) \\ |LP\rangle &= \frac{1}{\sqrt{2}}(|g,1\rangle - |e,0\rangle) \quad . \end{aligned} \tag{2.34}$$

For the cavity mode in resonance with the ISB transition, i.e. for vanishing detuning $\Delta = 0$, we find that the energies of the upper and lower polariton

$$E_{UP,LP} = \hbar\omega_{12} \pm \hbar\Omega \tag{2.35}$$

are separated by the so-called Rabi splitting $2\hbar\Omega$, in analogy to the avoided crossing behavior illustrated in Figure 2.2b. This energy splitting can be measured by FTIR spectroscopy, which will be discussed in section 3.5. Instead of a single peak due to the resonant absorption of the cavity, we then expect to find a double-peak corresponding to the upper and lower polariton. In this work we want to build a system, where the antiresonant terms in 2.31 are not negligible but rather of high importance. Thus, we consider the system to be originally in the state $|g,0\rangle$, which means we look what happens in the dark. For the RWA Hamiltonian immediately follows that the initial system state $|g,0\rangle$ at $t = 0$ is stationary, which can be emphasized by calculating the time evolution for small times $t > 0$

$$\begin{aligned} |\psi(t)\rangle &= e^{-\frac{i}{\hbar}Ht}\,|g,0\rangle \\ &\approx (1 - \frac{i}{\hbar}Ht)\,|g,0\rangle = |g,0\rangle \quad . \end{aligned} \tag{2.36}$$

However, if antiresonant interactions are accounted for we find that the time evolution of the system is given by

$$|\psi(t)\rangle \approx (1 - \frac{i}{\hbar}Ht)\,|g,0\rangle = |g,0\rangle - i\Omega t\,|e,1\rangle \quad . \tag{2.37}$$

The system evolves towards a state with an excited state contribution, which means we have a non-zero probability to find the electron in an excited state. But if so, the

system evolved into a state with higher energy, which means we need to discuss energy conservation in our system. We find that in order to fulfill energy conservation, the new system state must be an intermediate state, which is occupied only for a time frame compatible with energy-time uncertainty

$$\Delta E \Delta t \geq \hbar \tag{2.38}$$

which is given by

$$\Delta t \geq \frac{\hbar}{\Delta E} = \frac{1}{2\omega_{12}} \ , \tag{2.39}$$

where we inserted the energy of the double-excitation $\Delta E = 2\hbar\omega_{12}$. Within this time period, the system must undergo a transition to a state with the same energy as the inital state. If we consider the case of a MQW structure with localized QW ground states and for simiplicity only one excited state delocalized over all QWs, the electron within this time must relax back into one of the ground states by means of another antiresonant process corresponding to the term $\sigma_- a$ in the Hamiltonian. In order to enhance the probability that these two processes take place within the allowed time period, we want to enhance the transition rate. According to Fermi's golden rule the transition rate is proportional to the square of the absolute value of the transition matrix element $|T_{if}|^2$ which to first order reads

$$T_{if} = \langle \psi_f | \, V \, | \psi_i \rangle \tag{2.40}$$

where the perturbation V is the interaction Hamiltonian

$$H_{int} = \hbar\Omega(\sigma_+ a + \sigma_- a^\dagger + \sigma_+ a^\dagger + \sigma_- a) \ . \tag{2.41}$$

Thus, the transition rate is proportional to Ω^2. Tuning Ω corresponds to tuning the coupling strengh $\frac{\Omega}{\omega}$, which in turn scales as the square root of the corresponding transition wavelength [17]

$$\frac{\Omega}{\omega} \sim \sqrt{\lambda} \ , \tag{2.42}$$

which is an advantage, as we are interested in ISB transitions with a transition energy of 100 meV corresponding to a wavelength of $\lambda = 12.4$ µm. We therefore believe that our system is suited to observe transitions induced by vacuum fluctuations.

2.3 Dark Transport

As we learned that the antiresonant terms in the Hamiltonian can lead to spontaneous excitations in our system, we want to investigate the effect on the electronic transport. In Figure 2.3 a sketch of a MQW structure is shown. When a cavity photon excites a ground state electron which was previously localized in the QW, it undergoes a transition to a delocalized excited state. When a small bias is applied, the stucture is tilted and an excited state electron favours to fall down in one of the neighbouring QWs in transport direction. This process corresponds to an effective hopping transport, which enhances the total vertical transport through the structure. Thus, in the absence of real photons, the spontaneous coupling to virtual photons out of the vacuum can lead to a so-called dark transport and an enhanced conductivity of the structure.

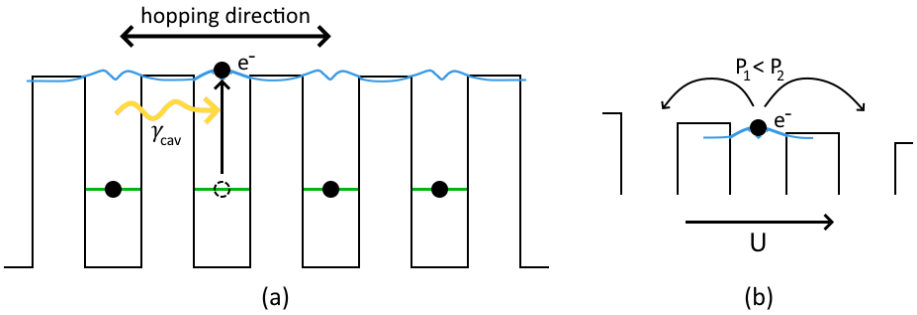

Figure 2.3: (a) Sketch of an ISB transition in a MQW structure, taking place as a cavity photon excites a localized ground state electron, which then occupies a delocalized excited state. Then, the electron relaxes again into one of the ground states, with a statistically distributed hopping direction. (b) When a voltage is applied, the structure is tilted, which leads to a preferred hopping direction and an effective transport.

Hence, when we measure the current through the structure we should, in fact, measure an enhanced current. But how can we determine the effect? If we accomplish to tune the dark transport, we would be able to measure relative changes in the conductivity of our samples. According to theoretical approaches the so-called compression factor η plays a crucial role for the strength of the effect [4]

$$\eta = \frac{V_{mode}}{\lambda_0^3} \quad , \tag{2.43}$$

where V_{mode} is the cavity mode volume and λ_0 is the free space wavelength of light resonant with the ISB transition. Thus, in this work our approach is to tune the compression factor in order to tune the influence of the vacuum fluctuations on the

conductance. As the wavelength of the ISB transition is fixed, our goal is to tune the mode volume. The cavity mode volume, in turn, depends on the occupied light mode. On resonance, light occupies a fundamental mode which corresponds to a small mode volume, whereas for higher order modes, the mode volume usually increases. Our goal is, thus, to build two different cavities. The first cavity shall be resonant with the ISB transition and the second cavity should favour a higher order mode of the same wavelength. In section 3.1.2 we will discuss the used cavity and how to tune its resonance. Another challenge is to distinguish the dark transport effect from other influences on the conductance. Especially in small structures the surface to volume ratio increases and, thus, surface effects start to play a role. We will discuss possible influences on the transport in section 4.3.

3 Methods

In this chapter, we will describe the samples investigated in this work and the methods used for the nanofabrication.

3.1 Description of Samples

3.1.1 Matter

In this work, we investigate structures based on alternating layers of GaAs and AlGaAs grown by Molecular Beam Epitaxy (MBE). These two materials have a similar lattice constant but different band gap energies and, thus, build a perfect material system for building quantum wells (QWs). The lower energy boundary of the quantum wells is built by the energy of the lowest conduction band in GaAs and the QW height depends on the difference of the respective band gap energies ΔE. The energy difference in turn depends on the aluminum fraction x of $Al_xGa_{1-x}As$, and is for $x < 0.45$ and at 300 K given by [18]

$$E_{dir} = 1.422 + x \cdot 1.248\, eV \tag{3.1}$$

$$\Delta E = x \cdot 1.248 eV \ . \tag{3.2}$$

In such a system, the transition between two discrete QW states is known as inter-subband (ISB) transition. As GaAs does not come with a high charge carrier density, n-type doping with silicon atoms acting as donors is applied to enhance the ground state occupation in the QWs. The first samples we investigated were two Resonant Tunneling Diode (RTD) structures, which are already known to exhibit interesting transport properties parallel to a strong coupling behavior [5]. The first RTD structure is highly doped (C0484) and is used to investigate the optical properties, whereas the second structure with undoped QWs (C0483) is designed for electrical measurements. The band structure was simulated for the second case with a Schrödinger-Poisson Solver and is shown in Figure 3.1. The thickness of the bare structure amounts to 210.8 nm, the full growth sheets are shown in the appendix. When a voltage sweep is applied, at some point the excited state of the first well aligns with the ground state of the second well, which leads to an enhanced tunneling probability and a tunneling peak in the measured current.

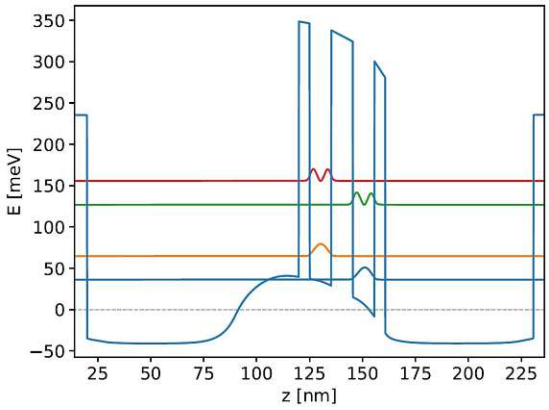

Figure 3.1: Simulated band structure of a Resonant Tunneling Diode structure with undoped QWs. When the structure gets tilted by an applied voltage, two respective QW states can align, which enhances the electron tunneling probability.

In further investigations the focus was laid on two Multiple Quantum Well structures. In these structures, the QW widths were chosen to suppress electron tunneling which lead to localized electronic ground states in the respective wells. However, the well width was chosen in such a way that the first excited states are already on the edge of the finite QW height and are correspondingly delocalized over multiple QWs. The first approach consists of five QWs with a low doping concentration and a bare thickness of 300.5 nm (C1299). The second approach is a structure with comparatively higher doping, only three QWs and a thickness of 199.5 nm (L1751B). In Figure 3.2 the simulated band structure of the two approaches is depicted. It has to be mentioned, that the two samples were grown by different groups independently. The growth sheets of the two structures are given in the appendix.

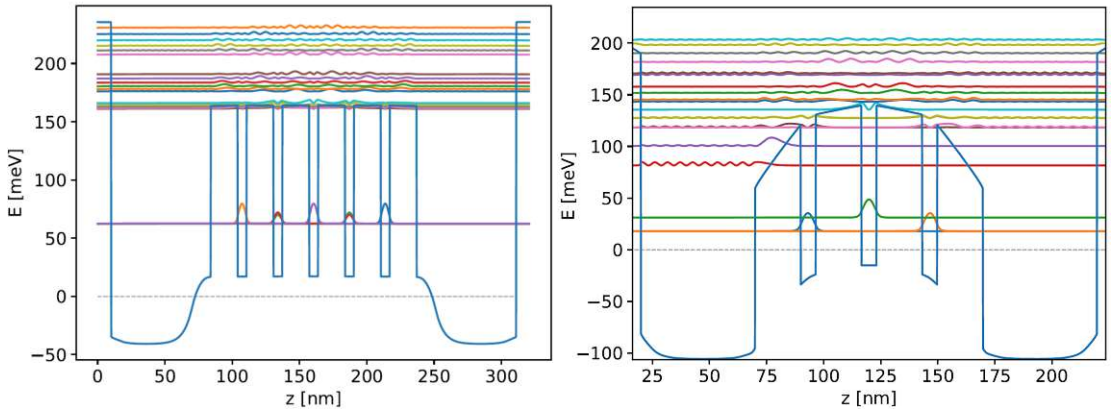

(a) C1299 **(b)** L1751B

Figure 3.2: Simulated band structure of two different designs for a MQW structure. The C1299 sample (a) has five quantum wells and the L1751B sample (b) has three quantum wells. Thus, they differ in structure thickness, but the quantum well widths and barrier thicknesses are equal.

Electrons occupying excited states are believed to contribute to the conduction of the structure when a bias is applied. However, at low enough temperatures only ground states are occupied and the conduction enhancement depends on electrons undergoing a transition to excited states. With this property a system is formed, where the electronic transport is influenced by the coupling to photons. Moreover, in the absence of real photons, the coupling to virtual photons emerging from vacuum fluctuations is, thus, believed to contribute non-negligibly to the physics of the system. However, to enable corresponding investigations we need to enhance the light-matter coupling strength of the system.

3.1.2 Photons

In order to couple light strongly to the intersubband transition, we need a cavity to enhance the light-matter coupling. By sandwiching our structure between two gold layers acting as mirrors, we build a so-called double-metal cavity, reminiscent of a Fabry-Perot resonator. At the same time, these layers enable an electrical contacting of the structure, which is important for our work. The gold layers in this case are separated by the sub-wavelength thickness of the structure. As we want the cavity to favor the ISB transition wavelength, we use the well-known concept of a micro patch resonator, which is built by shaping the top gold layer into a square with micrometer dimensions. We then use the square patch as an etch mask to shape the structure in

X- and Y-direction. A sketch of the resulting device architecture is shown in Figure 3.3.

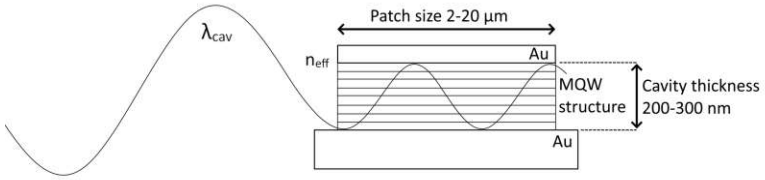

Figure 3.3: Sketch of a patch resonator based on a MQW structure embedded in a double metal cavity formed by two gold layers.

This leads us to a cavity with tunable resonance frequency which for a given structure depends only on the patch size and the relative permittivity [19]. We can now tune the patch resonance to hit the ISB transition. As shown above, our structures exhibit an ISB transition of 100 meV corresponding to light of 12.4 µm wavelength. For tuning the patch size to resonance, we first need a starting point. According to literature [19], the frequencies of the resonant modes in a micro patch resonator with metallic top and bottom contacts can be calculated from a cavity model, depending on the patch dimensions and material properties, and are given by

$$f_{mnp} = \frac{1}{2\pi\sqrt{\mu\epsilon}}\sqrt{\left(\frac{m\pi}{d}\right)^2 + \left(\frac{n\pi}{L}\right)^2 + \left(\frac{p\pi}{W}\right)^2} \ , \tag{3.3}$$

where d is the thickness of the bare structure, L is the length and W is the width of the patch. For thin structures d $\ll$ L and square patches L = W, we find the frequency of the dominant mode for m = p = 0 and n = 1

$$f_{010} = \frac{1}{2 \cdot L\sqrt{\mu\epsilon}} \ . \tag{3.4}$$

With a relative permeability of $\mu_r \approx 1$ and a relative permittivity of $\epsilon_r = 10.89$ for GaAs, we can calculate the necessary patch size for a wavelength of 12.4 µm

$$L = \frac{\lambda}{2 \cdot \sqrt{\mu_r \epsilon_r}} = 1.88\,\mu m \ . \tag{3.5}$$

Thus, by tuning the patch sizes from 1.0 µm to 2.0 µm in linearly spaced steps for the optical measurements, we at some point hit the ISB transition. By looking at the absorption properties of the device by FTIR spectroscopy a polariton splitting on resonance should be observable. However, as the absorption of a single patch resonator is not sufficient to be detected, patch resonator arrays (e. g. 100x100) are formed for

each patch size to enhance the total absorption. With the cavity design accomplished, we further pursue our goal to investigate the transport properties of the structure. For that, a voltage needs to be applied on a single patch resonator. This is not possible without an auxiliary structure for contacting, as typical needle tip radii for probing are already much larger than the optical patch size. Thus, the processing includes a subsequent run for building a contacting structure on top of the patch resonators.

3.1.3 Bridges

For electrical measurements on single patch resonators it is possible to cover the structure with silicon nitride (SiN) and build a contacting structure on top. The SiN will thereby act as electrical insulator. Afterwards, holes are etched into this layer and filled with gold, building a connection to the top gold of the patch resonator. Contacting patches on top of the SiN are then connected to the holes via bridges. At another site, the bottom gold layer of the patch resonators is being uncovered as well in the course of the hole etch. By contacting a single contacting patch and the bottom gold with two needles, the transport properties of the structure can be probed.

In summary, we formed a system that is designed for strong light-matter coupling and based on the structure of interest, which we believe to be perfectly suited for the study of the influence of vacuum fluctuations on the vertical transport. Furthermore, we want to probe these transport properties on single patch resonators by means of a contacting structure. The starting point of the sample processing is the design of the resonator layout which will be given in the next section. This is followed by a description of the nanofabrication process.

3.2 Layout of Resonators

In order to build the desired patch resonator structures, we first need to plan the layout of the resonators on the sample. The resulting mask is then transferred to the sample surface by means of photolithography. For the first processing run with the RTDs, we started to develop a mask by modifying an already existing one which contained bonding patches and optical arrays to enable electrical and optical measurements at the same time. While the bonding patches fill the upper part of the mask, the optical patch arrays are arranged randomly on the bottom and the patch size varies linearly spaced from 1.0 µm to 2.0 µm, as shown in figure 3.4. The first modification was the integration of 20 µm patches in between the bonding patches. Furthermore, another two mask layers were designed for the contacting structure on top, aiming at contacting

the 20 µm patches as well as individual 2 µm patches of the optical array. This modified 3-layer mask was used for investigations on the RTD with undoped QWs (C0483) and is shown in figure 3.4a. In parallel, the second RTD structure with doped QWs (C0484) was processed without building a contacting structure. The next modification of the mask extended the number of contacted 2 µm patches by replacing two of the optical patch arrays by 2 µm patch arrays. Moreover, 5 µm and 10 µm patches were included and contacted near the bonding patches. The resulting mask was used for the processing of the first MQW structure approach (C1299) and is depicted in 3.4b.

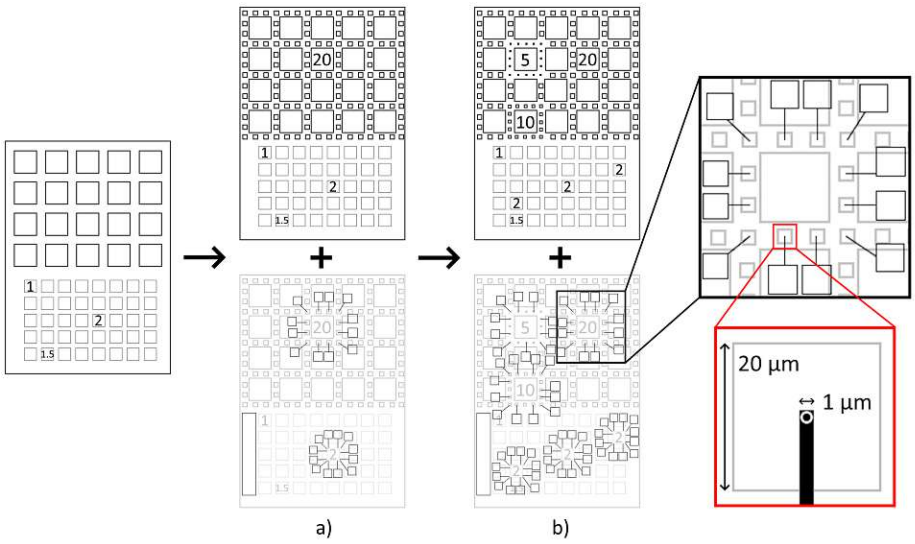

Figure 3.4: Sketch of two photolithography masks, derived from an original mask with bonding patches and optical arrays (left). **a)** At first, newly embedded 20 µm patches and individual 2 µm patches of the corresponding optical array were contacted by 1 µm-wide bridges with 120 µm length and contacting patches of 100x100 µm. **b)** Secondly, the number of contacted 2 µm patches was extended and patches of 5 and 10 µm size were included.

For the processing of the second MQW structure approach (L1751B), we decided to design a new mask from scratch, to include space for the contacting structure and, thus, avoid overlapping structures. In a more organized way, this mask again contains the square bases of the future patch resonators of various sizes, which is shown in figure 3.5.

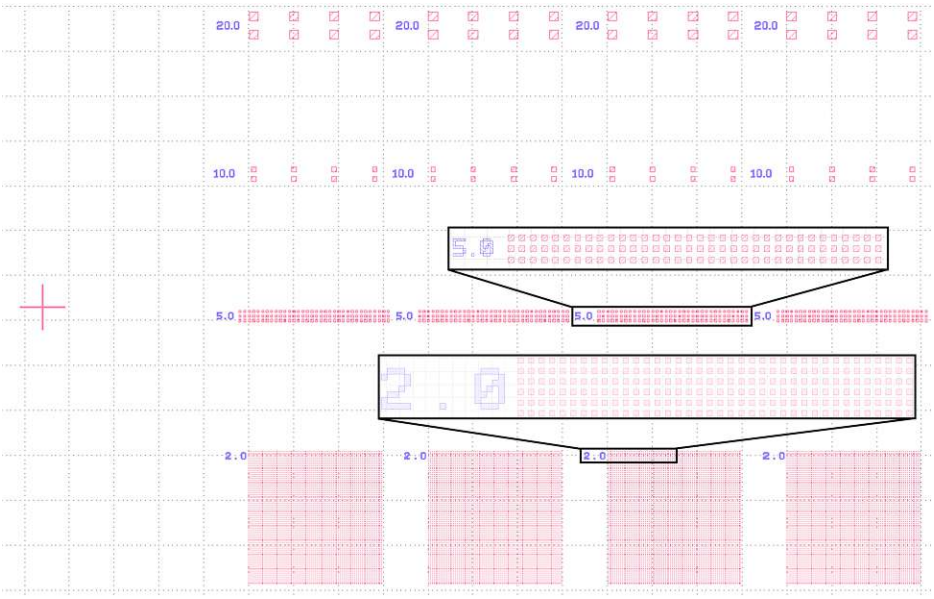

Figure 3.5: Section of the photolithography mask for the MQW sample L1751B with patches of four different sizes (2, 5, 10, 20 µm) and an alignment cross at the edge of the structure.

For the electrical measurements single patches have to be contacted through the SiN layer. To accomplish this, holes are etched into the SiN. The holes for the 2 µm patches have a diameter of 1 µm, whereas the holes for the other patch sizes were chosen to measure 3 µm. Furthermore, a large rectangle is embedded in the second mask layer to uncover a part of the bottom gold. The corresponding mask is shown in figure 3.6.

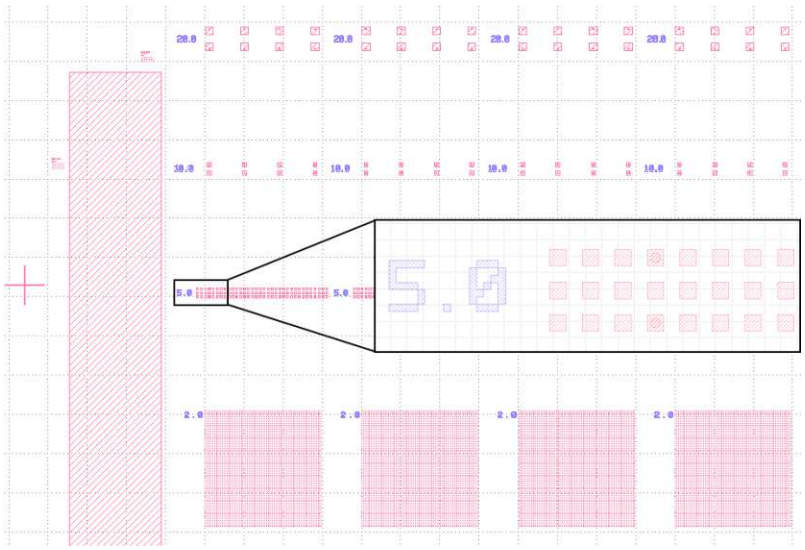

Figure 3.6: Photolithography mask for the holes etched into the SiN layer. Here, the mask was merged with the first mask for clarity. The rectangle on the left side enables a contacting of the bottom gold. Nearby, small test structures were included for a post-process evaluation of the quality of the etched holes. The inset shows two 3 µm-wide holes on 5 µm patches.

On top of the SiN layer, contacting patches and bridges to the holes are needed for the contacting. Therefore, a third mask was designed, which is depicted in figure 3.7. In the case of the 2 µm patches, the bridges are 2 µm wide and 10 µm long. For all larger patch sizes the bridges are 5 µm wide and again 10 µm long. The contact patches are of the size 80x100 µm. The alignment of the three masks happens through alignment crosses embedded in the masks. At least three crosses are necessary in order to hit the already present structures with maximum precision and to compensate for a relative sample rotation. All of the 10 and 20 µm patches included in the mask are contacted afterwards. For the 2 and 5 µm patches there are more patches included, than are contacted later on. This is helpful for an evaluation of the process quality during processing.

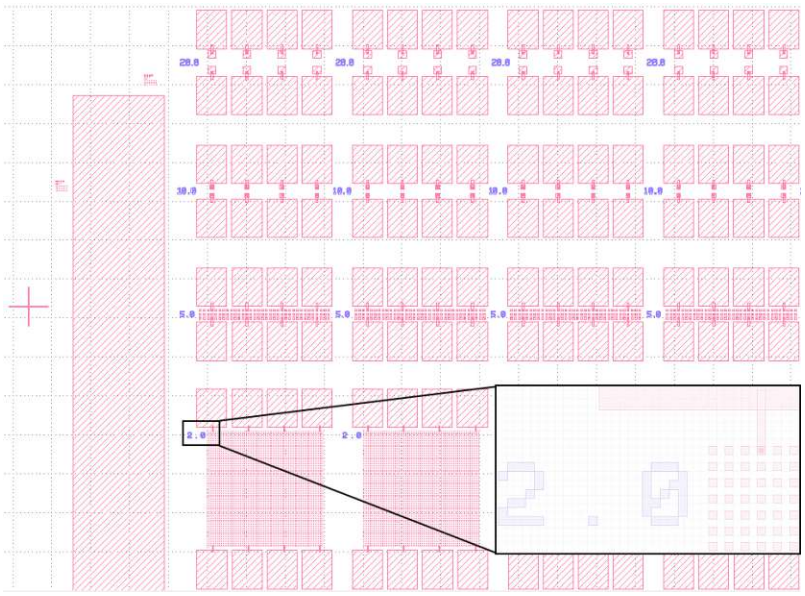

Figure 3.7: Photolithography mask for the contacting patches and bridges on top of the SiN layer. The mask was merged with the two previous masks. The inset shows the connection between a single 2 µm patch and the contacting patch over the bridge.

3.3 Nanofabrication process

The methods used for the nanofabrication of patch resonators based on a MQW structure, and for building a contacting structure on top, will be explained in the following. As the processing procedure was similar for all samples, the processing details of the RTDs will not be shown. An overview of the most important processing steps is given in Figure 3.8. At first, the sample is covered with a sputtered titanium-gold layer and bonded on a n-doped GaAs sample in order to build a stable device during the processing. Then, the uncovering of the hetero structure is achieved by means of polishing and wet etching with first, a mixture of ammonia hydroxide and hydrogen peroxide and, second, with hydrofluoric acid. In the next step, the mask for the patch resonator structure is transferred to the sample surface by photolithography and gets covered by an evaporated Ti-Au layer afterwards. Then, this layer gets structured by a lift-off process and serves as an etch mask for the subsequent RIE of the hetero structure.

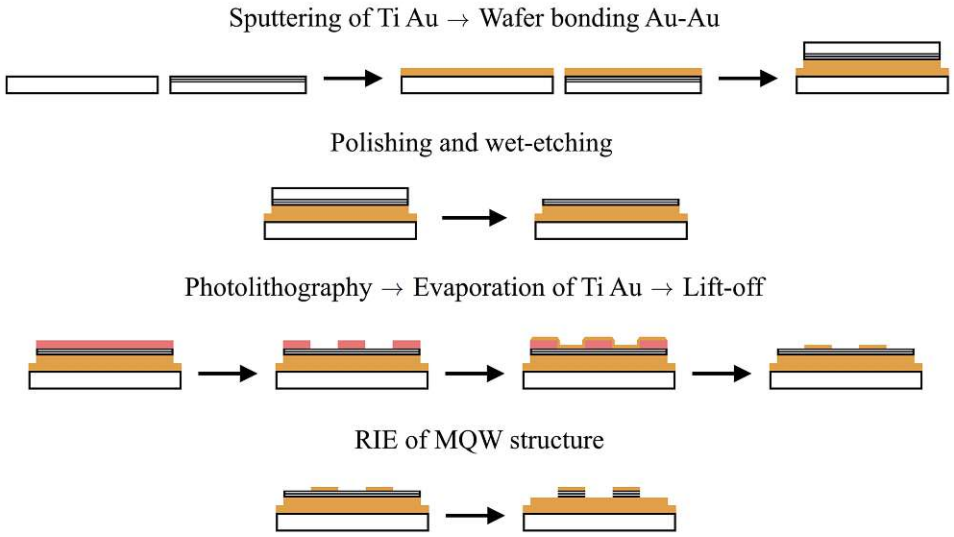

Figure 3.8: Overview of the main processing steps for the patch resonator structures. In the beginning, the left sample represents the n-doped GaAs substrate and the right sample depicts the MQW sample.

With this accomplished, the patch resonators are formed and the first part of the processing is done. Nevertheless, in this work we aim at contacting single 2 µm patches, which makes an auxiliary structure necessary. A sketch of the processes used for building the contacting structure is shown in Figure 3.9.

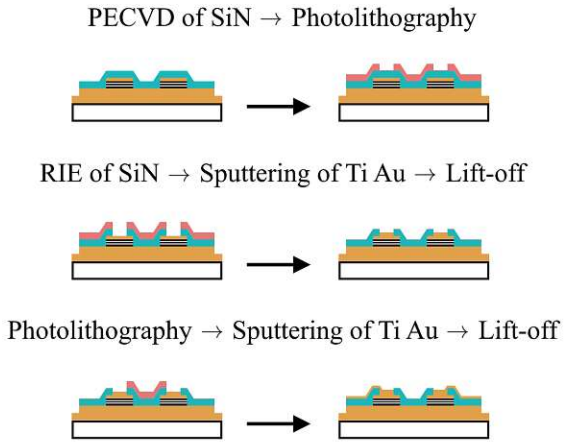

Figure 3.9: Overview of the main processing steps for building a contacting structure on top of the patch resonators with an insulating SiN layer in between.

The first step includes the covering of the patch resonators with a SiN layer, followed by the etching of holes into this layer. Then, by sputtering of Ti-Au and a subsequent lift-off, these holes are filled with gold. Finally, the contacting bridges and patches are built on top by another series of photolithography, sputtering and lift-off. In the following, the individual processing steps and the used parameters will be explained in more detail.

3.3.1 Ti-Au Sputtering and Wafer Bonding

As already mentioned above, the thinness of the MQW structure makes an Au-Au wafer bonding process necessary. In the course of that, a gold layer is sputtered on the top side of the substrate and the hetero structure sample. To enhance the bonding strength between GaAs and gold, a titanium layer is sputtered on the samples prior to the gold layer, in order to mediate the bonding. In the sputtering process a glow discharge creates an argon plasma, consisting of argon ions and electrons. Due to the negative bias of the target material building the cathode, the positively charged argon ions are accelerated towards the target. Through the momentum transfer of the ions hitting the target material, neutral atoms leave the target and depose on the sample surface [20]. After each sputtered layer, the sample gets cooled for 30 seconds to avoid an overheating. The parameters of the sputtering step for the wafer bonding are shown in table 3.1.

Sputter Parameters Wafer Bonding

Material	Power	Layers	Step time	Rate	Final layer thickness
Ti	100 W	1	60 s	-	-
Ti	30 W	1	60 s	8.4 nm/min	8.4 nm
Au	30 W	29	60 s	34.2 nm/min	991.8 nm

Table 3.1: Parameters of the sputtering process of a titanium-gold layer with a Creavac sputtering system. The first line represents a titanium oxide removal step for cleaning the target. After each sputtered layer, the sample is cooled for 30 seconds.

It has to be mentioned that for the RTDs and for C1299 a different sputtering system (Von Ardenne) was used. However, for all samples the parameters were tuned accordingly to achieve similar layer thicknesses in the course of the different sputtering steps. After the sputtering, the two samples are bonded together by the Au-Au interface. To accomplish that, the hetero structure sample is flipped and placed on the substrate

sample. Then, the combined sample is being warmed up, and a force is applied in Z-direction over a specified amount of time. The wafer bonding parameters used are shown in table 3.2.

Wafer Bonding

Z-force	Temperature	Step time
1350 N	330 °C	3 h

Table 3.2: Parameters for the Au-Au wafer bonding process.

The sputtered gold layer of the wafer bonding process will also serve as bottom gold contact for the patch resonators. With the newly formed sample, the next step is the uncovering of the hetero structure. This is achieved by polishing and wet-etching.

3.3.2 Polishing and Wet Etching

First, the sample is polished with a 35 µm-coarse polishing paper until only a 50-100 µm thin layer of the hetero structure sample remains. The rest of the substrate layer, which covers the hetero structure, has to be removed by a wet-etching step. Thereby, a 1:20 mixture of ammonia hydroxide (NH_4OH) and hydrogen peroxide (H_2O_2) is used to remove GaAs. In reaction with hydrogen peroxide, GaAs builds an oxide which then is dissolved by ammonia hydroxide [21]. This process comes with a high selectivity regarding the aluminum fraction x of $Al_xGa_{1-x}As$. Thus, $Al_{0.55}Ga_{0.45}As$, which has a significantly lower etch rate for this process than GaAs, is used as an etch stop layer. After removing the GaAs over the course of 30-40 minutes, the etch stop layer is being removed itself by a dip into hydrofluoric acid (HF). The HF etching process in turn also comes with a high selectivity. Thus, the GaAs contact layer of the bare hetero structure coming to light is not attacted by the HF. Finally, the bare hetero structure remains on top of the bonded substrate and the sample is ready for the photolithography.

3.3.3 Photolithography

For the photolithography the sample is covered with photoresist, deposed by spin coating. On a baking plate at 100 °C, the photoresist hardens for one minute. Afterwards, it gets exposed by the Laser Writer (Heidelberg Instruments) according to the designed mask. In this work we used a dose of 110 mJ/cm^2. Then, on the exposed sites the photoresist vanishes in the course of a developing step. The next step includes the

evaporation of a Ti-Au layer followed by a lift-off process for structuring the deposed layer.

3.3.4 Ti-Au Evaporation and Lift-off

For a higher uniformity of the top contacts, the titanium-gold layer is deposed by evaporation instead of sputtering. To ensure a high deposition quality, the sample is dipped into hydrochloric acid just before the process, to remove any present oxide layer on the hetero structure surface. During the process, the target material gets heated up by an electron beam and the evaporated atoms condense on the sample surface afterwards. The deposition rate can be controlled by the emission current of the electron beam. In the beginning, the rate is slowly ramped up with the emission current, while the shutter is still closed. During the process, the rate is tracked by an oscillator crystal, whose resonant frequency shifts with the thickness of a deposed material on top. Thus, also the thickness of the deposed layer is being tracked and the process finishes automatically, when the desired layer thickness is reached. The used parameters for the evaporation process are depicted in table 3.3.

Evaporation of Ti Au

Material	Rate	Final layer thickness
Ti	0.05 nm/s	10 nm
Au	0.1 nm/s	60 nm

Table 3.3: Parameters for the evaporation of a titanium-gold layer with a Plassys Evaporation system. Due to the necessary warm-up of the deposed materials prior to the evaporation, no titanium-oxide removal step is needed.

The resulting Ti-Au layer is then structured by a lift-off process. In the course of that, the underlying photoresist is being dissolved by a remover substance e. g. acetone. On the sites covered with photoresist, the Ti-Au gets ripped off while the photoresist dissolves. The layer only survives on sites without photoresist, where it sticks to the hetero structure. With this accomplished, the top contacts for the patch resonators are built, which also serve as an etch mask for the subsequent RIE process.

3.3.5 Reactive Ion Etching

For shaping the hetero structure into patch resonators, we use an Inductively Coupled Plasma - Reactive Ion Etch (ICP-RIE) process. As already mentioned above, the struc-

tured gold layer on top is used as an etch mask. For this process, the plasma is generated by a magnetic field powered by the set radiofrequency (RF). The cathode carrying the sample is connected to the RF via a capacitor and, thus, the electrons cannot drain off. This leads to a negative bias potential of the cathode accelerating the ions towards the sample. As a consequence, the preferential etching direction is the growth direction of the sample (Z-direction), as the physical-chemical etch reaction depends on the kinetic energy of the plasma ions. Additionally, in the case of ICP-RIE, an RF-coil is used to couple energy into the plasma, leading to an enhanced generation of etch-reactive particles. Thus, by setting the RF and ICP power, ion energy and plasma density can be controlled separately [20]. Moreover, the use of $SiCl_4$ leads to a passivation of the sidewalls of the structure, which suppresses the etching in X- and Y-direction even further [22]. The anisotropy of this process is important for the vertical etching of the GaAs/AlGaAs hetero structure used to form the patch resonators. The process parameters are visible in table 3.6.

ICP-RIE parameters

Step time	RF power	ICP power	$SiCl_4$	N_2	Set pressure	Strike pressure	Table temp.
13 min	55 W	20 W	7 sccm	17 sccm	3 mtorr	40 mtorr	20 °C

Table 3.4: Parameters for the ICP-RIE process of the hetero structure with an Oxford Instruments RIE Plasmalab system. The sample holder is cooled during the process to remain at 20 °C. The step time includes an overetching period to obtain vertical sidewalls.

After this etching process, the construction of the patch resonators is completed and we proceed with the contacting structure.

3.3.6 Contacting Structure

In the following, we describe the necessary processing steps for building a contacting structure for single patch resonatos. The first step includes the covering of the whole structure with an isolating SiN layer. This is accomplished by Plasma-Enhanced Chemical Vapour Deposition (PECVD). The process parameters for the deposition of SiN are listed in table 3.5.

PECVD SiN

Step time	RF Power	SiH_4	NH_3	N_2	Rate	Final layer thickness
30 min	20 W	875 sccm	20 sccm	500 sccm	12.5 nm/min	375 nm

Table 3.5: Parameters of the PECVD of SiN as insulating covering on top of the patch resonators with an Oxford Instruments PECVD system.

After the SiN layer is formed, again, photolithography is used to build a mask for the etching of holes into the layer. This is accomplished by another RIE process with the parameters given in table 3.6.

SiN Etch Parameters SF_6

Step time	RF power	SF_6	Set pressure	Strike pressure	Table temperature
10 min	60 W	40 sccm	15 mtorr	40 mtorr	38 °C

Table 3.6: Parameters of the SF_6-based RIE process for etching holes into SiN with an Oxford Instruments RIE Plasmalab system.

It should be mentioned that for the RTDs and for C1299 a different, but very comparable RIE process for the etching of holes into the SiN layer has been used. The corresponding parameters can be found in table 3.7.

SiN Etch Parameters CHF_3

Step time	RF power	CHF_3	Pressure	Table temperature
7 min	150 W	50 sccm	75 mtorr	20 °C

Table 3.7: Parameters of the CHF_3-based RIE process for etching holes into SiN with an Oxford Instruments RIE Cobra system.

The holes are placed on top of the patch resonators in order to contact the top gold. For that, we fill the holes with another sputtering process of titanium-gold with the parameters given in table 3.8. Compared to the sputter process for the wafer bonding, the sputter parameters used for this step have been modified. The process now starts with a plasma-cleaning step of the sample surface. Furthermore, the step time per layer has been reduced to 30 seconds to prevent the sample from reaching high temperatures.

Sputter Parameters Holes

Material	Power	Layers	Step time	Rate	Final layer thickness
-	50 W	1	60 s	-	-
Ti	100 W	1	60 s	-	-
Ti	30 W	2	30 s	8.4 nm/min	8.4 nm
Au	30 W	10	30 s	34.2 nm/min	171 nm

Table 3.8: Parameters of the sputter process used to contact the top gold of the patch resonators through SiN holes with a Creavac sputtering system. The first line corresponds to a plasma-cleaning process of the sample surface. Compared to the sputtering process shown above, the step time per layer has been reduced.

After the sputtering, we again remove unwanted parts of the Ti-Au layer by the lift-off. Then, another photolithography process with the third mask is used to build the contacting structure on top of the SiN. Again, a layer of Ti-Au is sputtered on the sample with the parameters in table 3.8. Finally, after a last lift-off step, the bridges and contacting patches on top of the SiN are formed and the processing is concluded. We can now apply a voltage on a specific contacting patch and the bottom gold in order to measure the vertical current through a single patch resonator.

3.4 IV measurements

The IV characteristics of the patch resonators are measured with a cryogenic probe station mounted on a vibration damped table. A sketch of the measurement setup is shown in figure 3.10 augmented by a camera picture of the sample being probed in figure 3.11. First, the sample is placed on the sample holder in the vacuum chamber, which is then pumped until a pressure of $\approx 10^{-6}$ mbar is reached. Then, the helium cooling is applied, which effects the sample holder and, thus, the sample being in thermal contact with it. When a stable temperature of about 4.3 K is reached, two needles are slowly placed on the contact patches and the bottom gold, as shown in figures 3.10 and 3.11. Finally, a Source Measure Unit (SMU) is used to apply a voltage sweep and measure the resulting current through the structure. When the cold measurements are concluded, the helium cooling is removed and the sample is starting to warm up. During the warm up time, another measurement series is performed in the temperature range 110-125 K. As a last step, room temperature measurements are taken after an overnight warm up. Beside the transport properties, also the optical properties of the sample under investigation are of high interest.

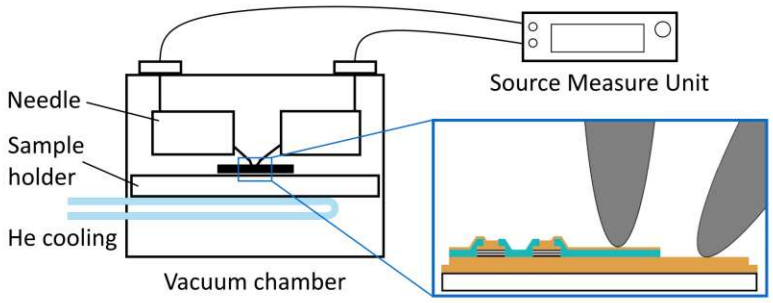

Figure 3.10: Setup for the transport measurements using a Cryogenic Probe Station combined with a Source Measure Unit and helium cooling applied. The inset shows two probing needles positioned at the contacting patch (left) and the bottom gold (right).

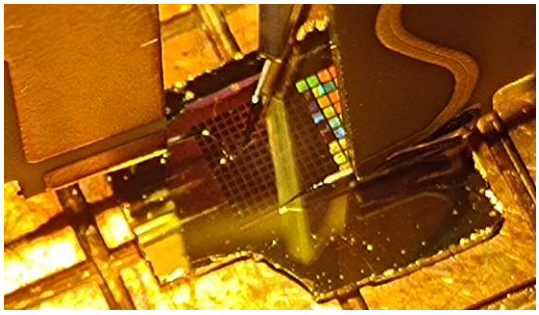

Figure 3.11: Camera picture of the inside of the probe station with the sample lying on the sample holder being probed by three needles. On the right side of the sample the characteristic colorful bragg reflections of the optical patch arrays are visible.

3.5 FTIR spectroscopy

Strong light-matter coupling manifests in a characteristic optical behavior of a sample. By FTIR spectroscopy, the absorption properties of a structure can be measured, which we utilize to observe strong coupling. Patch resonators are known to have a resonant wavelength, which depends on the patch size. This property enables a tuning of the absorbed wavelength by tuning the patch size, which we accomplish by including optical patch arrays of different size on the sample. During the measurement, for each of these arrays a single FTIR spectrum is recorded, which we expect to show the resonant absorption line. By recording the spectrum we tune the energy of the incident light over an energy interval, which includes the intersubband transition energy of 100 meV. When the patch resonance overlaps with the transition energy, electronic

and photonic states hybridize and lead to emerging polaritons in the system. The anticrossing leads to an upper and lower polariton state resulting in a double peak in the spectrum. The measurement setup includes a Bruker Hyperion microscope with an embedded FTIR-spectroscope and a liquid nitrogen-cooled Mercury-Cadmium-Telluride (MCT) detector. The source for the mid-IR light is a resistively heated SiC globar. FTIR spectroscopy utilizes an interferometer to form an interferogram based on the incident light. In reflectivity measurements the light is reflected on the sample and suffers from absorption losses before it is detected. Then, the absorption spectrum can be calculated from the detected interferogram by Fourier Transformation. For the detection of light with mid-IR wavelength by an MCT detector, the adjustable direct bandgap of $Hg_{1-x}Cd_xTe$ is utilized, leading to wavelength sensitivities in the range 0.7 to 25 µm. The sensitivity thereby depends on the cadmium fraction x. Furthermore, for a certain cadmium fraction, the resulting cut-off wavelength of the detector depends on the temperature. Thus, by cooling the detector to 77 K, the sensitivity can be extended to higher wavelengths [23].

4 Results

In this chapter, the results of the sample processing are presented, followed by the measurements of the optical and transport properties.

4.1 Processing Results

The processing of the MQW samples C1299 and L1751B was monitored by the microscope, with images taken between the most important steps. Different optical contrast and colouring of the images correspond to different microscope settings. The first evaluation was performed after the photolithography. The formed 2 µm patch arrays of both samples are presented in Figures 4.1a and 4.1b.

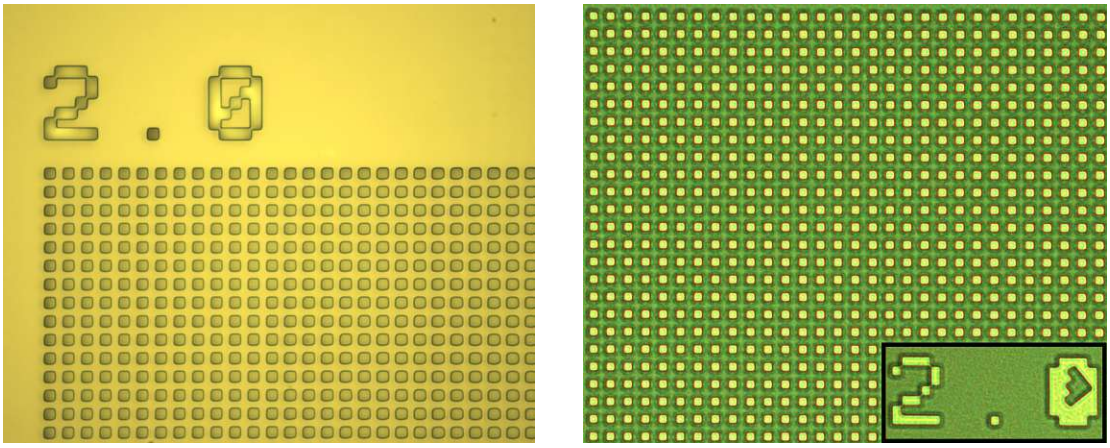

(a) C1299 **(b)** L1751B

Figure 4.1: Close-up microscope images of 2 µm patch arrays in the structured photoresist layer on top of the heterostructure surface after the exposure in the course of photolithography.

Overview images of the samples after the photolithography are given in Figures 4.2a and 4.2b. In Figure 4.2a optical arrays of C1299 are visible and Figure 4.2b shows patches of different sizes in L1751B, according to the mask in Figure 3.5.

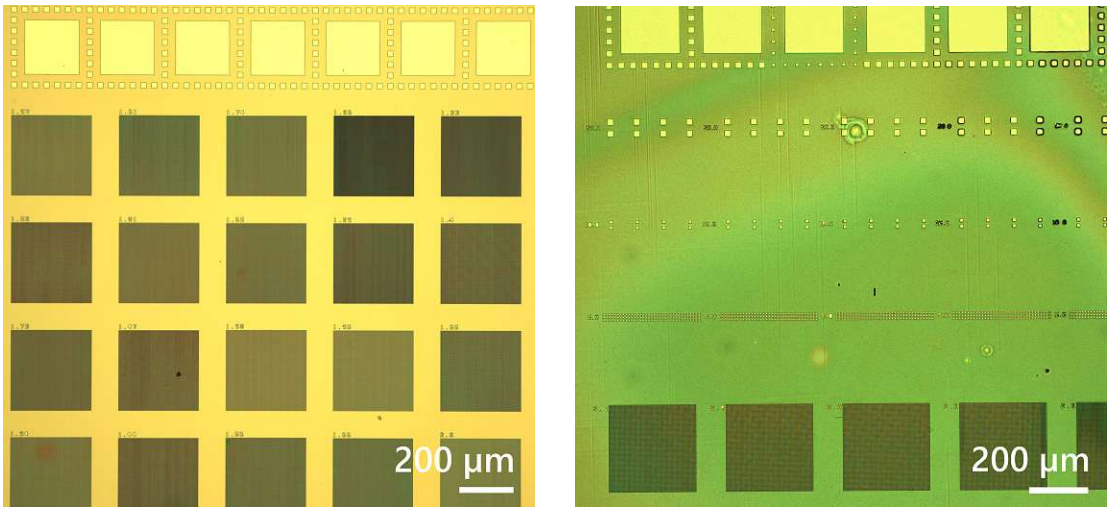

(a) C1299 **(b)** L1751B

Figure 4.2: Overview of the samples after the photolithography. (a) The optical patch arrays needed for the tuning of the patch resonance are visible. (b) Different patchsizes were formed, with blank spaces in between for later added contacting patches.

After etching the heterostructure, the images in Figures 4.3a and 4.3b were taken, which show the fabricated 2 µm patch resonators with the Ti-Au layer on top. In between the structures, the bottom gold layer is visible.

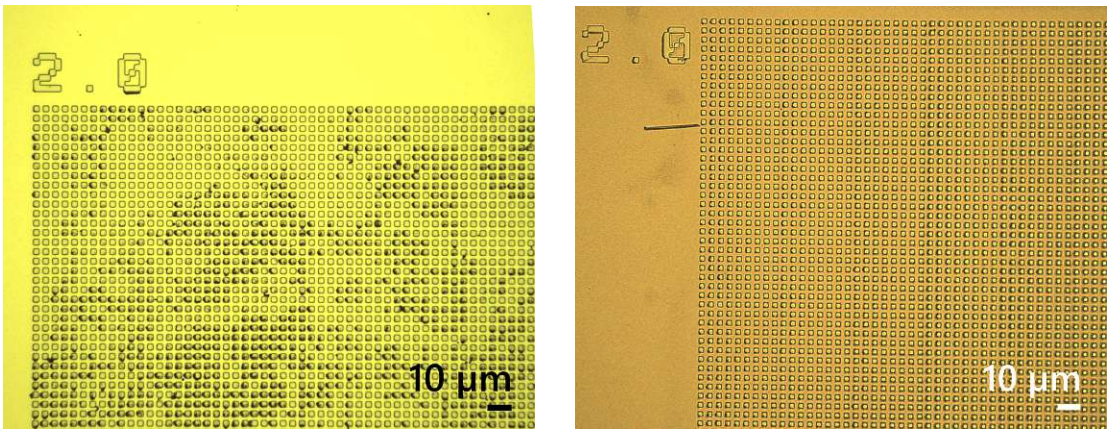

(a) C1299 **(b)** L1751B

Figure 4.3: 2 µm patch resonator arrays after the vertical etching of the heterostructure.

In Figures 4.4a and 4.4b overview images of the two samples are depicted, which show that the fabrication of the planned structures according to the designed photolithography masks was successful.

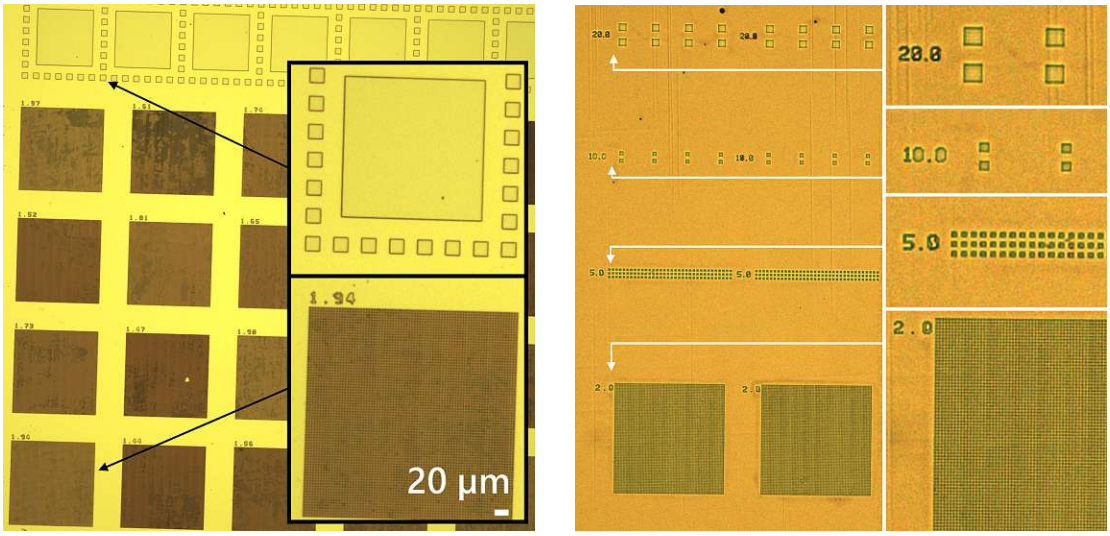

(a) C1299 **(b)** L1751B

Figure 4.4: Microscope images of the samples after the heterostructure etching. The insets show (a) 20 µm patch resonators surrounding a bonding patch of 200 µm size and a single optical array with a patchsize of 1.94 µm, (b) patch resonators with different patchsizes of 2, 5, 10 and 20 µm.

Figure 4.5 shows a Scanning Electron Microscope image of a fabricated 2 µm patch resonator based on a C1299 sample. The sample was mounted on a tilted holder to enable an evaluation of the processed sidewalls of the structure. It confirms that the used RIE process led to a good vertical shape of the resonators and demonstrates the quality of the nanofabrication process.

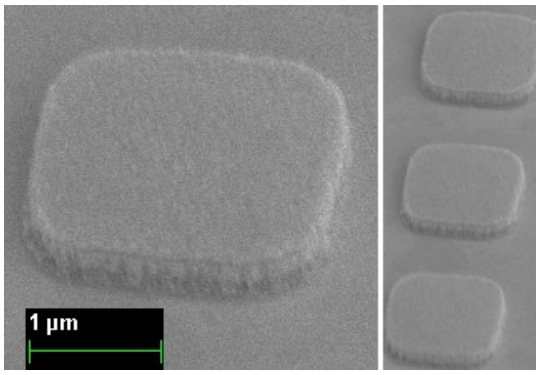

Figure 4.5: Scanning Electron Microscope image of 2 µm patch resonators based on a C1299 structure.

The subsequent fabrication of the contacting structure included the covering of the finished patch resonator structures with SiN. After etching the holes into the SiN layer, the photoresist was removed in the case of C1299. For L1751B, an additional sputtering and lift-off step was performed prior to the photoresist removal, to deposit gold in the holes. For both cases microscope images were taken afterwards, which are shown in Figures 4.6a and 4.6b.

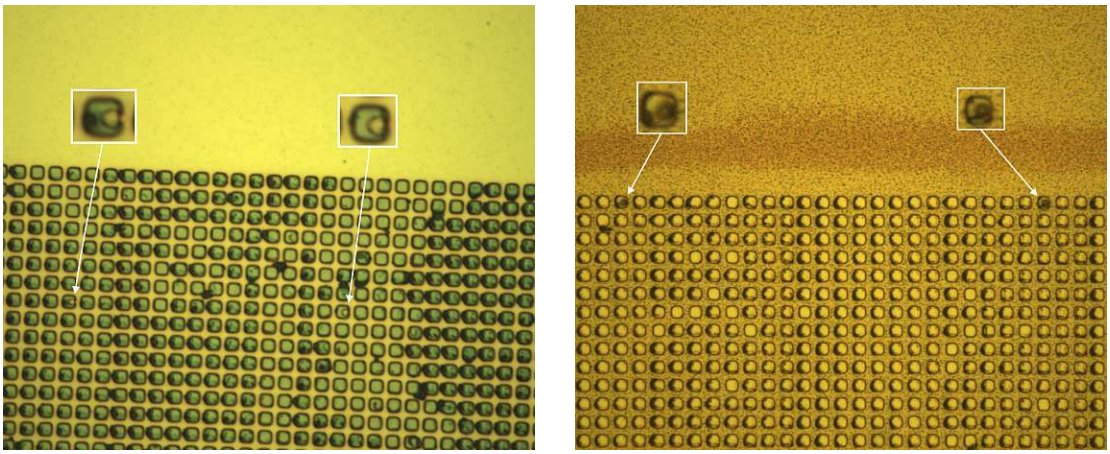

(a) C1299 **(b)** L1751B

Figure 4.6: 1 µm holes etched into the SiN layer on top of 2 µm patch resonators for the electrical contacting. The holes in both samples are slightly off-centre.

The 5 µm patch resonators of both samples are depicted in Figures 4.7a and 4.7b. The hole diameter is 1 µm in the case of C1299, whereas in L1751B the holes are 3 µm wide.

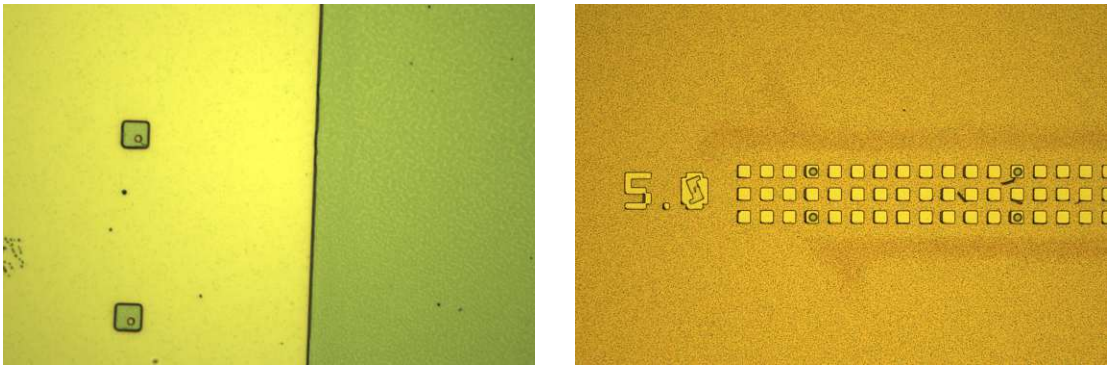

(a) C1299 **(b)** L1751B

Figure 4.7: 5 µm patch resonators with (a) 1 µm and (b) 3 µm wide holes etched into the SiN layer on top.

After a further series of photolithography, sputtering and lift-off steps, the processing of the contacting structure was completed. Microscope images taken afterwards are shown in Figures 4.8a and 4.8b.

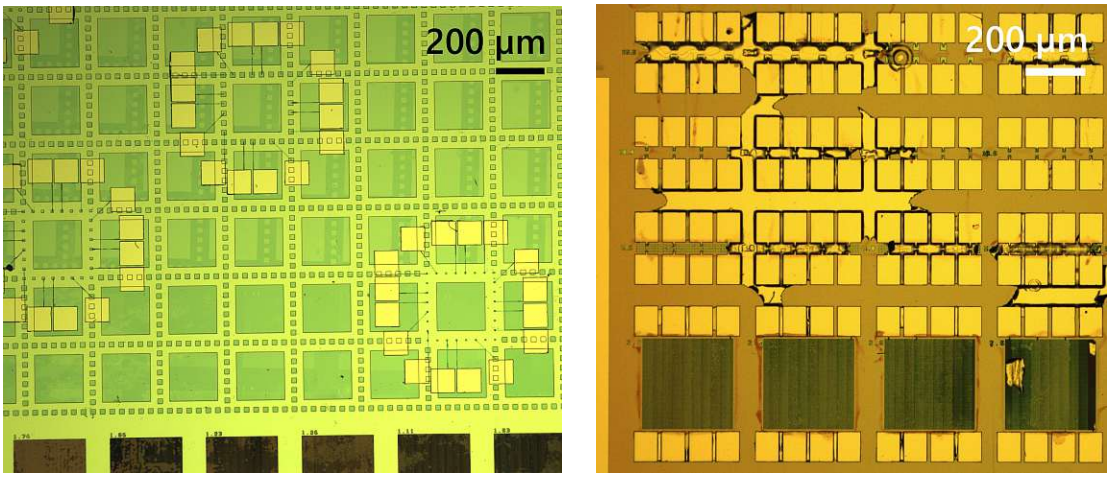

(a) C1299 **(b)** L1751B

Figure 4.8: Microscope images of the samples after the processing has been completed. (b) In L1751B gold residues from the lift-off step for the contacting structure remained between some of the contacting patches.

In both samples, the lift-off process led to problems, making an ultrasound bath step to remove gold residues necessary. Using minimal power we were able to largely remove the gold layer. Thereby, in the case of C1299 the gold was removed completely, but many of the contacting bridges were ripped off, leading to a reduced number of contacted patch resonators. Thus, we modified the bridge dimensions in L1751B, which lead to many patch resonators accessible for electrical measurements, even though the gold layer could not be removed completely. Figures 4.9a and 4.9b show 2 µm patch resonators of the two samples, which were contacted successfully.

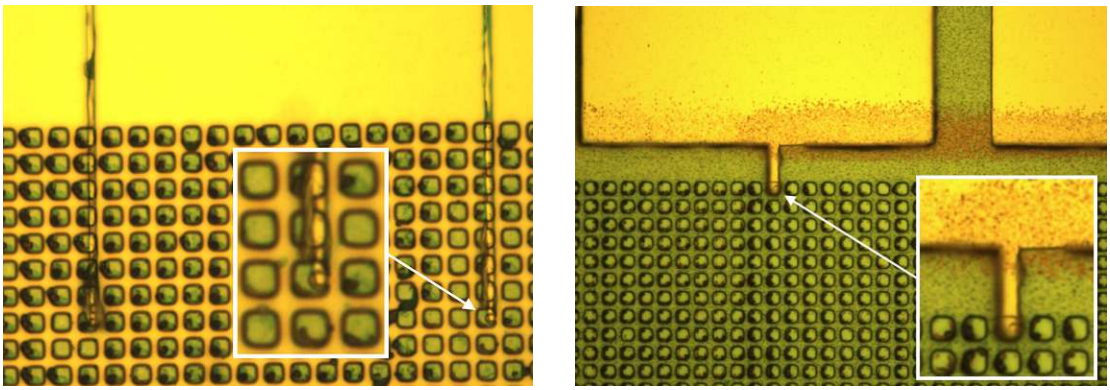

(a) C1299 **(b)** L1751B

Figure 4.9: 2 µm patch resonators contacted by different bridges. (a) 120 µm long and 1 µm wide bridges were built on top of an already existing structure covered by SiN. (b) 10 µm long and 2 µm wide bridges were built on the even SiN layer.

Finally, close-up images of micro patch resonators with patchsizes 5, 10 and 20 µm based on L1751B are shown in Figure 4.10.

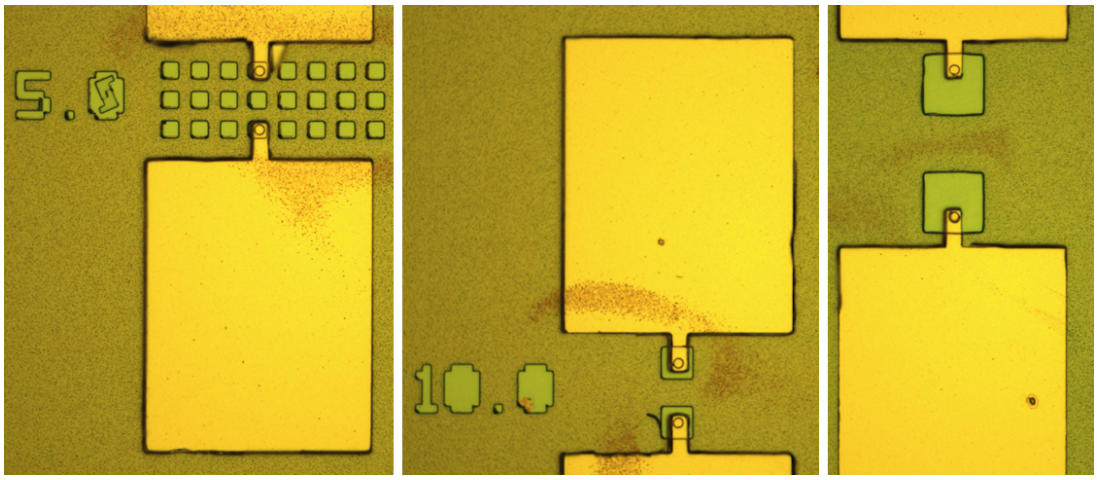

Figure 4.10: Microscope images of contacted patch resonators in L1751B with a patchsize of 5, 10 and 20 µm. All bridges are 5 µm wide and 10 µm long.

4.2 Optical Properties

Since our goal in this work is to investigate transport effects in strongly coupled RTD and MQW structures, we used a nanofabrication process to embed these structures in micro patch resonators, in order to achieve a strong light-matter coupling. By measuring the absorption spectrum of the fabricated devices by FTIR spectroscopy, we can examine the functionality and tunability of the cavities and look for polaritons in the structure. Furthermore, the presence of a Rabi splitting provides valuable information about the coupling strength and the ISB transition in the investigated sample. Thus, we performed optical measurements on doped samples, including measurements on a predecessor MQW structure which was processed prior to the structures we focus on in this work. The structure contains an inherent ISB transition of 100 meV and 21 QWs according to a cavity thickness of 485.5 nm. By a similar processing procedure as described above, the tuning of the resonance frequency of the micro patch resonators was accomplished by building resonator arrays with patchsizes in the range 1.5 to 3.0 µm with a step size of 0.024 µm. The measured absorption spectrum is shown in Figure 4.11.

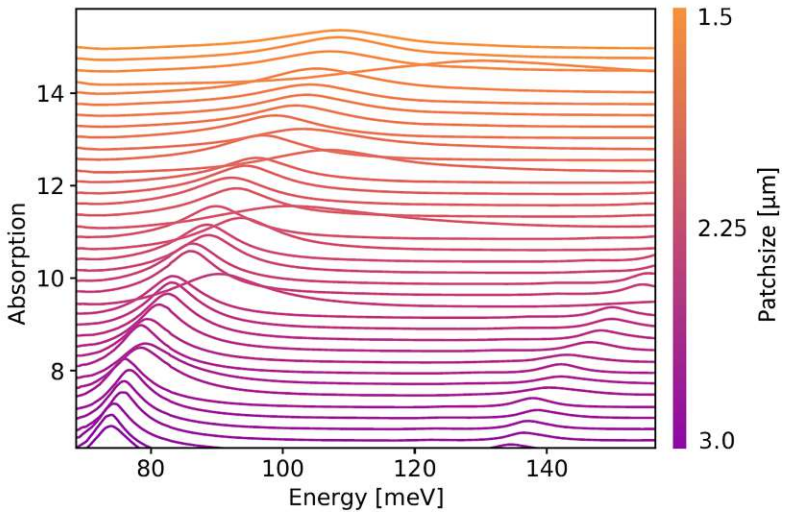

Figure 4.11: FTIR spectroscopy measurement of a highly doped MQW structure with optical patch resonator arrays in the range 1.5 to 3.0 µm. The resonance frequency is tuned by the patchsize resulting in shifted absorption peaks. Higher order modes emerging for energies above 135 meV show the same behavior.

The respective graphs correspond to measurements on single optical arrays. The average difference in patchsize between two adjacent curves amounts to ~0.04 µm, due to the reduced number of measurements after data analysis. In the measured absorption spectrum we observe the expected tuning of the cavity resonance with corresponding energies in the range 75 to 110 meV. In section 3.1.2 we used the cavity model to calculate the patchsize which leads to resonance with an ISB transition of 100 meV to 1.88 µm. In the absorption spectrum we identify a patchsize of ~1.8 µm, which is in good agreement. Above 135 meV, higher order modes of the cavities start to emerge. The measured mode spacing confirms the validity of the single mode approximation we used in deriving the Jaynes-Cummings Hamiltonian in section 2.2. Overall, we proved the success of the nanofabrication process for building micro patch resonators based on a MQW structure and were able to demonstrate the functionality and tunability of the resonators, although we did not observe a strong coupling.

4.2.1 RTD C0484

In the search for polaritons we performed FTIR spectroscopy measurements on the doped RTD structure C0484. The processing of this sample included the fabrication of optical arrays with patchsizes in the range 1.0 to 2.0 µm with a step size of 0.016 µm. The structure leads to a cavity thickness of the micro patch resonators of 210.8 nm. In Figure 4.12, the measured absorption spectrum is depicted, where after data analysis the average difference in patchsize between two graphs amounts to ~0.03 µm. We observe absorption lines of the micro patch resonators which are tuned by the patchsize, verifying their functionality and tunability, and identify a large mode spacing, which even exceeds the fundamental cavity mode energy. Furthermore, near 100 meV we observe a clear polariton splitting due to resonance of the cavity with the ISB transition, resulting in a double-peak in the measured spectrum.

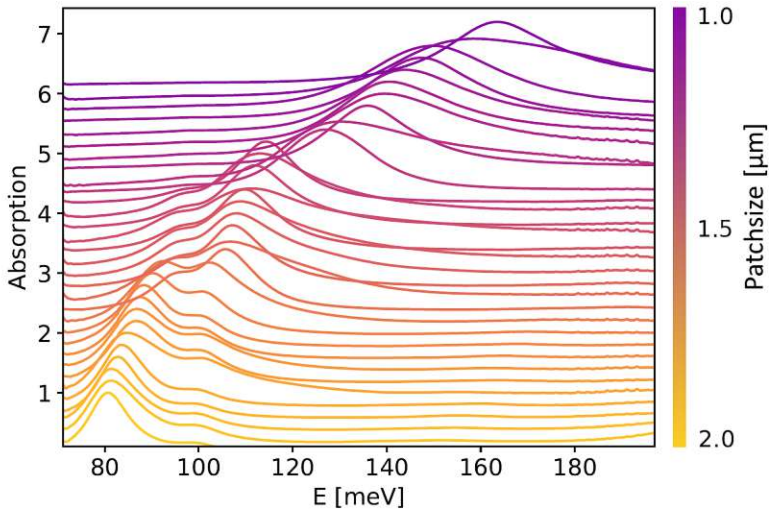

Figure 4.12: FTIR spectroscopy measurement performed on the RTD structure. The resonator patchsize scales from 1.0 to 2.0 µm. The spectrum shows a clear polariton splitting near 100 meV for a patch size of ~1.65 µm. The upper and lower polariton energies amount to 102.2 and 92.5 meV.

We identify the upper and lower polariton energies to be 102.2 and 92.5 meV, from which we obtain the Rabi splitting

$$2\hbar\Omega = 9.7\,meV \tag{4.1}$$

and the corresponding coupling strength of $\frac{\Omega}{\omega} \approx 0.05$. This proves a strong light-matter coupling in the sample and allows us to identify the patchsize of ~1.65 µm which leads to resonance with the ISB transition. It is smaller than the value of 1.88 µm calculated by

the cavity model, but still in a rather good agreement, given the simplicity of the model. From the position of the double-peak we obtain information on the ISB transition which corresponds to 97.3 meV. Moreover, we are able to determine the cavity Q-factor given by the ratio of the peak position and the full width at half maximum

$$Q = \frac{\omega}{\Delta\omega} = \frac{E}{\Delta E_{FWHM}} = 9.3 \tag{4.2}$$

and find that the polariton splitting is still present in micro patch resonators with a patchsize of 2 µm. This observation provides a solid basis for the study of transport effects in 2 µm resonators caused by the coupling of electrons to virtual photons, which will be discussed in the following.

4.3 Transport Properties

The IV measurements performed on the RTD and MQW structures will now be presented.

4.3.1 RTD C0483

In addition to the optical measurements performed on the doped RTD C0484 we also studied the transport properties of the undoped RTD C0483. In Figures 4.13a and 4.13b the current measured in single 2 µm and 20 µm patch resonators at 4.3 K is shown. Contrary to expectations, no resonant tunneling peak was observed in the transport of the 2 µm resonators. The current at 2 V is of the order of ~0.1 nA. In the measurement on the 20 µm resonator at an applied voltage of 1.9 V a clear resonant tunneling peak is visible. The peak height of 0.7 µA corresponds to an enhancement of the current of ~63 % which is due to the alignment of the excited state level of the first QW with the ground state level of the second QW where the electrons are injected, as already mentioned in section 3.1.1.

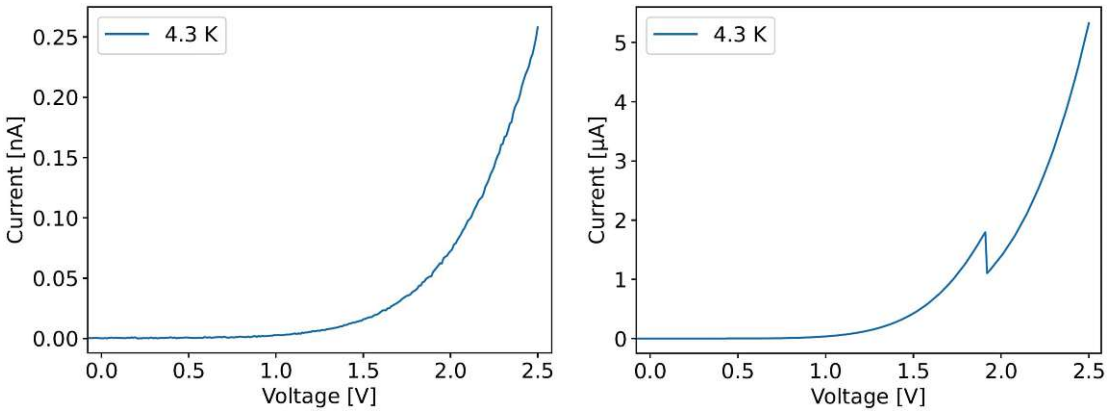

(a) 2 µm **(b)** 20 µm

Figure 4.13: IV characteristics of 2 µm and 20 µm patch resonators measured at a temperature of 4.3 K. (a) In 2 µm patch resonators no resonant tunneling is observed, whereas in (b) 20 µm patch resonators a clear tunneling peak emerges at 1.9 V.

The measured current densities of 2 µm and 20 µm patch resonators at a temperature of 4.3 K are compared in Figure 4.14.

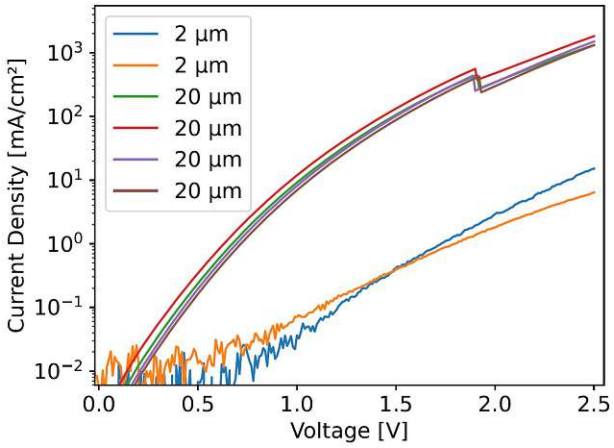

Figure 4.14: Current density of 2 µm and 20 µm patch resonators at a temperature of 4.3 K. For a patch size of 2 µm the current density is reduced by two orders of magnitude compared to the 20 µm case.

All of the 20 µm resonators show a resonant tunneling peak at a similar voltage position, in contrast to the 2 µm resonators, where no resonant tunneling is observed. Furthermore, we find that the current densities for different patchsizes differ by two

orders of magnitude. The strongly reduced current density for 2 µm patch resonators compared to the 20 µm case in the RTD structure was not expected. Assuming that processing features have led to smaller dimensions, the planned 1 µm holes used for the contacting of the 2 µm patch resonators and the long and only 1 µm wide bridges could, in principal, cause a throttling of the current. However, this is probably not the case, as the 20 µm patch resonators have been contacted in the same way, while exhibiting a larger current. With the same argumentation we can also exclude photoresist residuals which harm the quality of the contacts as a possible cause. By considering the geometric aspect we find that the influence of the surface is a possible explanation. Surface effects can play a role, as the surface to volume ratio $\frac{A}{V}$ increases for decreasing patch size, where for the area A we only consider the lateral surface. The band structure of a material can be deformed at the surface, which on the one hand, can cause surface channels for electrons enhancing the current or, on the other hand, can lead to surface states in which electrons get trapped, which reduces the current. Thus, surface effects could explain the reduced transport in 2 µm resonators by a trapping of electrons. By considering vacuum fluctuations we find a second possible explanation. A current reduction due to a dark transport is against our statements about such effects in section 2.3. However, this is not a contradiction as the RTD structure differs significantly from the MQW structures. It includes a single spacer layer which for a positive voltage is reached by the electrons not until overcoming the two QWs separated by the thick tunneling barrier. As we derived earlier, through a coupling of virtual photons to the ISB transition, the excited state occupation in the two QWs is enhanced. Since the tunneling probability for excited state electrons is larger, we believe that for small voltages it is likely that electrons tunnel out of the QWs through the thin barriers. We find that for an electron in the second QW the energy gained by tunneling into the contact layer against transport direction is much higher than the energy gained by an electron in the first QW which tunnels into the spacer layer. The gained energy in turn determines the probability, which is why we believe that a transport reduction due to a dark transport may be the case, which in combination with current reducing surface effects would explain the large gap between the 2 µm and 20 µm current densities. By considering the order of the current density in 20 µm resonators and the reduction in the 2 µm case by a factor of ~100, we estimate the upper boundary for the strength of the present effects to ~1 A/cm^2.

In Figure 4.15, the temperature dependence of the current in a single 20 µm patch resonator is shown. Even at room temperature, the resonant tunneling manifests in the curvature of the graph near 2 V. The peak is washed out since due to the thermal energy many electrons are able to overcome the structure without the need for tunneling.

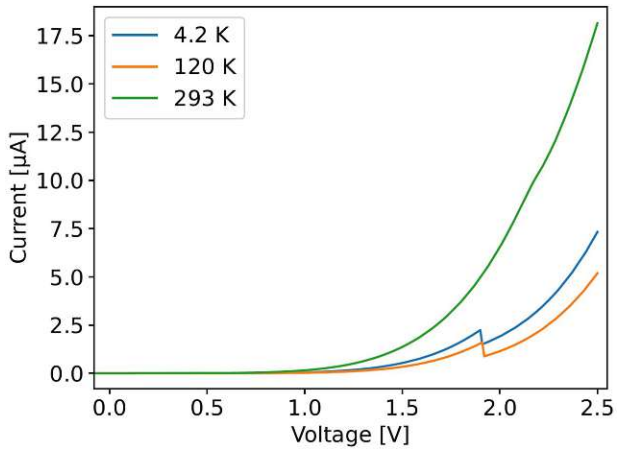

Figure 4.15: Temperature dependence of the current of a single 20 µm patch resonator. The tunneling peak is visible at low temperatures and is washed out at room temperature, still manifesting in a change of the curvature. The room temperature current density is increased by less than one order of magnitude compared to the 4.3 K case.

With the newly gained information about the room temperature behavior of the transport, we consider again Figure 4.13a. The missing tunneling peak at 4.3 K can not be understood by means of processing artifacts. Thus, we consider vacuum-induced excitations as a possible cause. Since vacuum effects are believed to be much larger in 2 µm resonators compared to 20 µm resonators, it is feasible that a dark transport leads to an out-washing of the tunneling peak by enhancing the excited state occupation. Since excited state electrons, have a higher tunneling probability than ground state electrons, it is possible that a number of excited electrons tunnel through the thick barrier already before the critical voltage of the state alignment is reached, and even more so after exceeding it. This enhancement of the current density apart from the expected tunneling peak position could explain the observed out-washing of the tunneling peak in 2 µm resonators.

4.3.2 MQW C1299

The IV measurements performed on single micro patch resonators with four different patchsizes based on the MQW structure C1299 are presented in the following. Single measurements on the current in 2 µm and 20 µm resonators at 4.3 K are shown in Figures 4.16a and 4.16b. The graphs reveal the expected exponential shape due to tunneling and are very smooth.

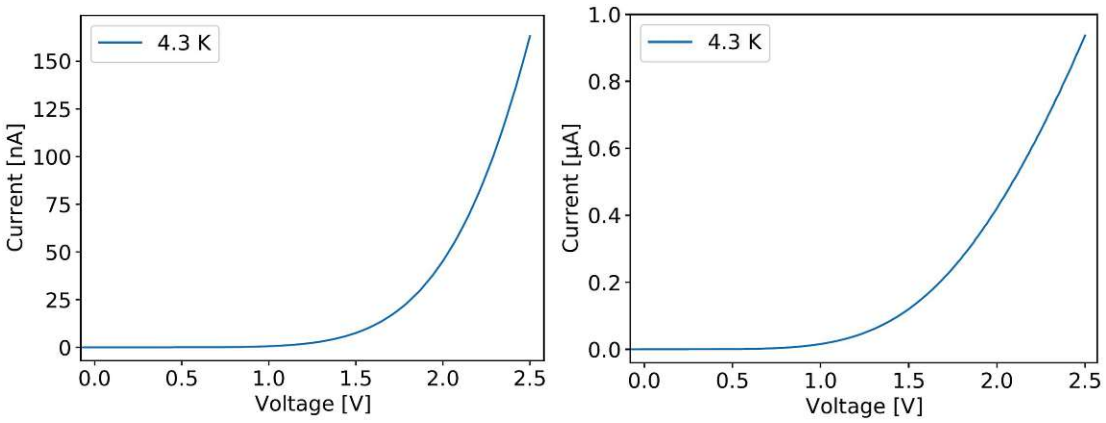

(a) 2 µm **(b)** 20 µm

Figure 4.16: IV characteristics of single 2 µm and 20 µm patch resonators measured at a temperature of 4.3 K.

In Figure 4.17 the current density mean values for the different patchsizes of 2, 5, 10 and 20 µm at 4.3 K are presented, which were calculated based on a number of 4, 3, 5 and 7 measurements. The current densities spread over two orders of magnitude, which was not expected. At high voltages the mean values are biased towards higher values as the standard deviation increases with voltage. However, the data reveals a clear correlation between the current density and the patchsize except for the 2 µm case. For a patchsize of 5, 10, and 20 µm we find current densities that decrease with patch size, which we believe is caused by surface effects.

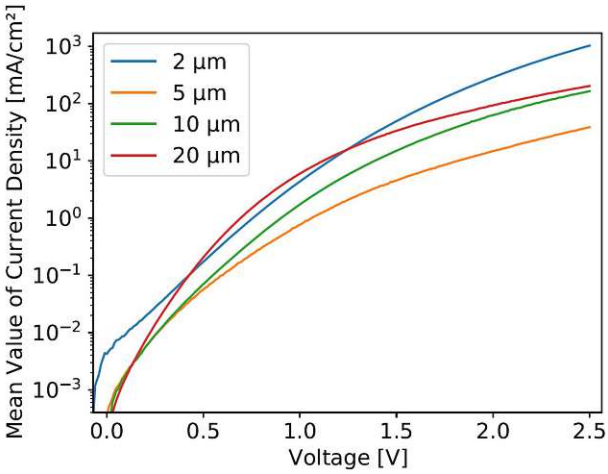

Figure 4.17: Current density mean values of patch resonators of different size at a temperature of 4.3 K.

For low voltages, the standard deviation is much lower and the 2 µm patch resonators show a significantly enhanced current density compared to other patch sizes. This is emphasized in Figure 4.18, which shows the current density mean values and the respective error bars for a voltage of 0.15 V. An accomplished t-test comparing the measured 2 µm and 20 µm patch resonator current densities reveals the difference is significant with a p-value of $0.0008 < 0.05$.

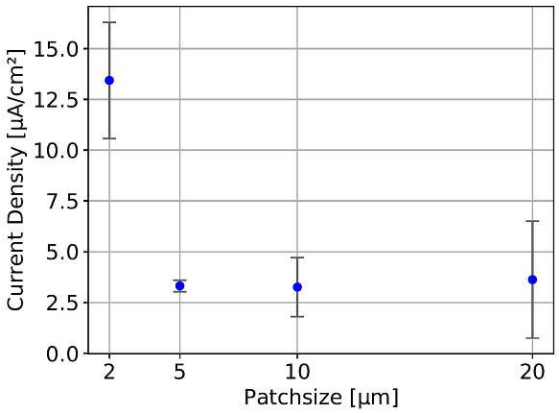

Figure 4.18: Mean current densities of patch resonators of different size at an applied voltage of 0.15 V and 4.3 K. The error bars show the standard deviation of the measurements. While the current density is similar for 5, 10 and 20 µm, it is significantly enhanced for a patch size of 2 µm.

The large spread in the measured current densities for high voltages could be explained by photoresist residuals harming the quality of the contacts. However, this could lead to a current reduction or a linear contribution in the measured current, but can not lead to a current enhancement. Furthermore, it has to be mentioned that we already excluded measurements showing a current density with a linear contribution in the course of data analysis. In general, a transport enhancement due to processing artifacts is unlikely, unless it leads to shortcuts. This leaves us with the question, how the current in 2 µm patch resonators can be surprisingly high. As we believe that a coupling of virtual photons to the ISB transition could lead to an enhanced current in C1299, we now examine if this is in accordance with our measurements. When the bandstructure is deformed due to an applied voltage, we believe the dark transport increases with the preferential hopping direction as already mentioned in section 2.3. We expected to find the largest effect strength in 2 µm patch resonators, which at low voltages and 4.3 K indeed show an enhanced current density compared to all other patch sizes. Another goal was to show that the effect strength can be tuned by the patch size. From the cavity model already mentioned in section 3.1.2, we can calculate the resonant modes with the corresponding energies for each patchsize by simply scaling the integer numbers n and p (setting m = 0). Near the ISB transition energy we find the fundamental mode of the 2 µm patch resonator. A 5 µm patch resonator does not exhibit a mode in the vicinity of the ISB transition and, thus, it represents the off-resonant case. Thus, we expect the highest effect strength in 2 µm patch resonators, whereas the 5 µm patch resonators should not show an effect at all. For the 10 µm and 20 µm patch resonators we already find a number of modes near the ISB transition, as the mode density increases with the mode order. Assuming the tuning of the effect strength by the cavity mode volume, we expect to find a smaller effect strength in these resonators compared to the 2 µm case, but we do not make a statement for which of the two the effect will be stronger, since in the 10 µm case the modes are of lower order, but in the 20 µm case more modes can contribute to the effect. Indeed, in C1299 the 10 µm and 20 µm current densities are larger than in the 5 µm case, perfectly matching the predictions. In our understanding, at low voltages only the 2 µm current density stands out, since for all other patch sizes the effect is negligible. At high voltages we estimate the maximum effect strength for a dark transport in 2 µm patch resonators to be of the order of ~1 A/cm^2. In contrast to the RTD structure this estimation does not include surface effects as they are of opposite sign in C1299. Thus, compared to the RTD the effect in C1299 can be larger, which meets our expectations since this sample was optimized for the study of a dark transport.

In Figure 4.19 the temperature dependence of the current measured in a single 20 µm patch resonator is depicted. The room temperature current is about four orders of magnitude higher than the current at 4.3 K.

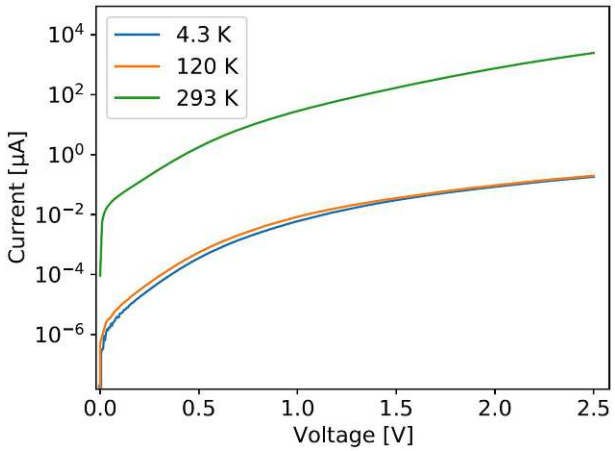

Figure 4.19: Temperature dependence of the current in a single 20 µm patch resonator.

The high temperature dependence of the current density in C1299 is reasonable as the conductivity in this sample due to the very low doping is strongly influenced by the enhancement of the charge carrier number caused by the thermal energy. At the same time such a behavior indicates a higher dark transport contribution relative to the total current, since the conductivity, as in the case of thermal excitations, should also be strongly influenced by virtual excitations. This, in turn, would explain the large spread in current density between resonators of different patchsizes observed in C1299.

4.3.3 MQW L1751B

The measurements performed on the MQW structure L1751B are presented in the following. In Figure 4.20 the measured currents in single 2 µm and 20 µm patch resonators are depicted.

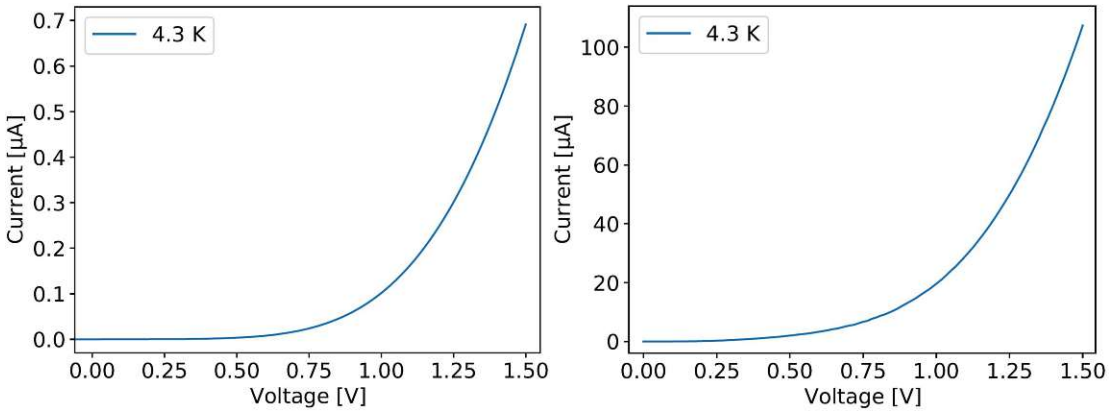

(a) 2 µm **(b)** 20 µm

Figure 4.20: IV characteristics of single 2 µm and 20 µm patch resonators at a temperature of 4.3 K.

We measure smooth graphs for the current which show the expected exponential behavior of the transport and no linear contributions, which indicates a good quality of the fabricated contacts. From the current density measurements performed at 4.3 K on single patch resonators with patchsizes 2, 5, 10, and 20 µm, the mean values of the current density were calculated based on 3, 3, 6 and 5 measurements. The results are shown in Figure 4.21.

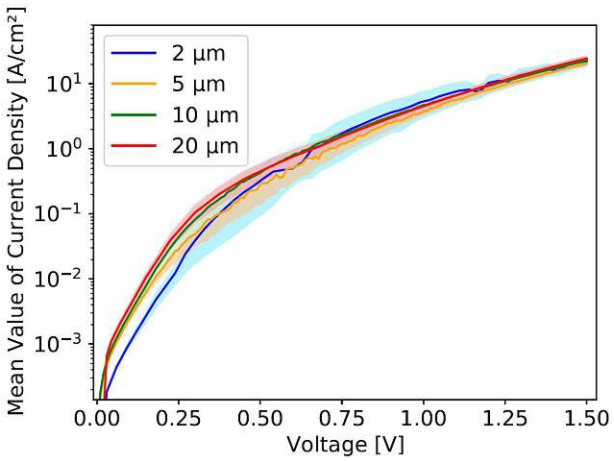

Figure 4.21: Current density mean values of patch resonators of different sizes at a temperature of 4.3 K. The shadow of a curve represents its standard deviation.

The shadows represent the respective standard deviations of the graphs of similar color. At low voltages, the 2 µm current density is reduced significantly compared to other

patch sizes, whereas at about 0.8 V the 2 µm current density exceeds all other curves. The dents in the 2 µm curve come from a single measurement which suffered from needle jumps. For high voltages, all patch sizes show a consistent current density. We repeated the measurements at room temperature and collected the data depicted in Figure 4.22.

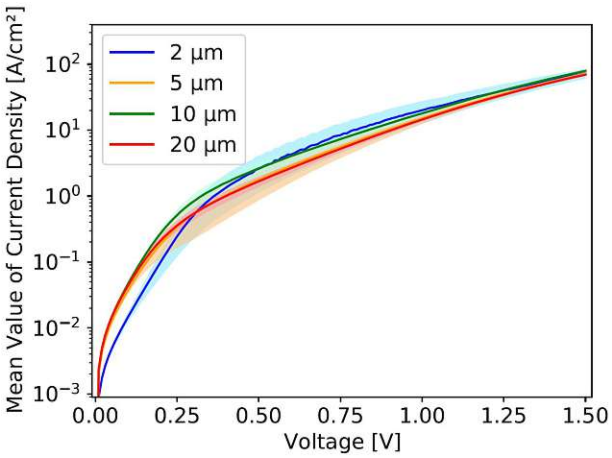

Figure 4.22: Mean current density of patch resonators of different sizes at room temperature. The shadow of a curve represents its standard deviation. For low voltages, the 2 µm patch resonator shows a reduced current density compared to other patch sizes. For high voltages, the current density is consistent for all patch sizes.

The current densities show the same behavior as in the low temperature case, with values increased by less than one order of magnitude. By considering voltages in the range 0.1 to 0.3 V we find the behavior depicted in Figure 4.23a. The measured current densities show a clear patchsize dependence. This result is emphasized in Figure 4.23b, which shows the calculated trendline for the mean current density values at 0.15 V.

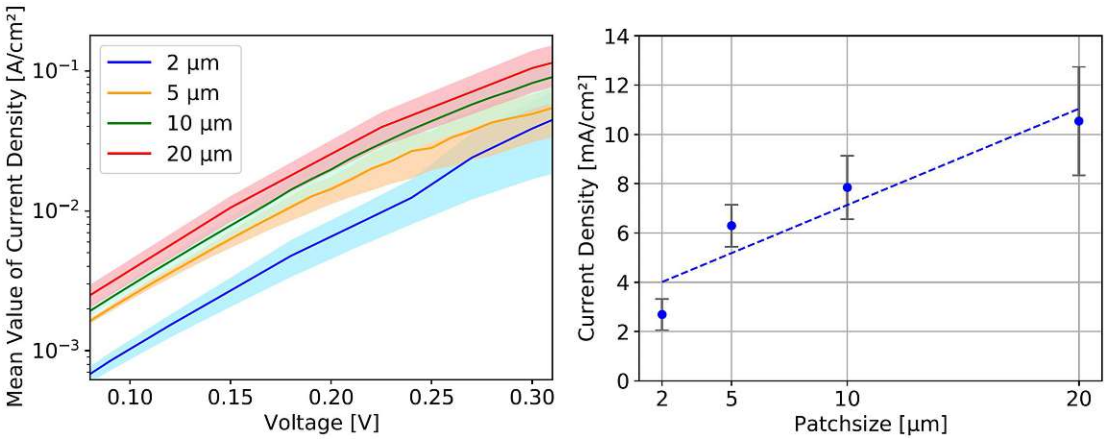

(a) (b)

Figure 4.23: Current density mean values of patch resonators with different sizes at a temperature of 4.3 K. (a) In the range of 0.1 to 0.3 V the standard deviations of the measured current densities are small, revealing a clear patchsize dependence. (b) At an applied voltage of 0.15 V, the trendline shows that the current density decreases with the patch size.

The 2 µm and 20 µm current densities differ significantly, according to a t-test with a p-value of $0.002 < 0.05$. This is also the case at room temperature, with a p-value of $0.0009 < 0.05$. Based on the clear trend and good consistency of the measured data, we believe that surface effects which appear in our samples reduce the current in smaller resonators. In the search for an explanation for the enhanced current density of the 2 µm resonators for voltages above 0.8 V we consider the possibility of a surface channel. This current enhancing influence of the surface could emerge when a certain voltage is reached, leading to the enhanced current we observe in the 2 µm resonators. However, this explanation is very unlikely, since the trendline is constant for this voltage range and the current density of the 5 µm resonators is lower than for all other patch sizes, contradicting a present surface channel. Thus, we interpret the observations by a dark transport. To understand the influence of vacuum effects on the 2 µm patch resonators we have another look on the bandstructure of L1751B in Figure 3.2b. The dome-like shape of the MQW structure due to the missing spacer layers, could lead to an attenuation of the preferential direction of the dark transport for a low applied voltage. In the case of C1299, all QWs are of equal height for $V = 0$ and, thus, already for a small applied bias we find a strong preferential direction. In contrast, for a dome-like shape at low voltages a large part of the electrons will still hop against transport direction destructing the expected vacuum-induced transport enhancement. A certain voltage

must be reached before the dome-like shape diminishes and the hopping effect happens preferably in transport direction and contributes to the current. In combination with the present surface effects this could explain the behavior of the 2 µm current density, which lags behind all other patch sizes at lower voltages and overtakes them at higher voltages. At maximum, the 2 µm current density exceeds the other curves by ~1 A/cm², perfectly matching with the estimated effect strength in the case of C1299. The fact that the 2 µm patch resonators show a similar current density compared to the other patch sizes at higher voltages is reasonable as for current densities of order ~10 A/cm² and higher, the dark transport according to our estimation becomes negligible. At the same time this indicates a good consistency of the measurements. The temperature dependence of the current in single 10 µm and 20 µm patch resonators is shown in Figures 4.24a and 4.24b.

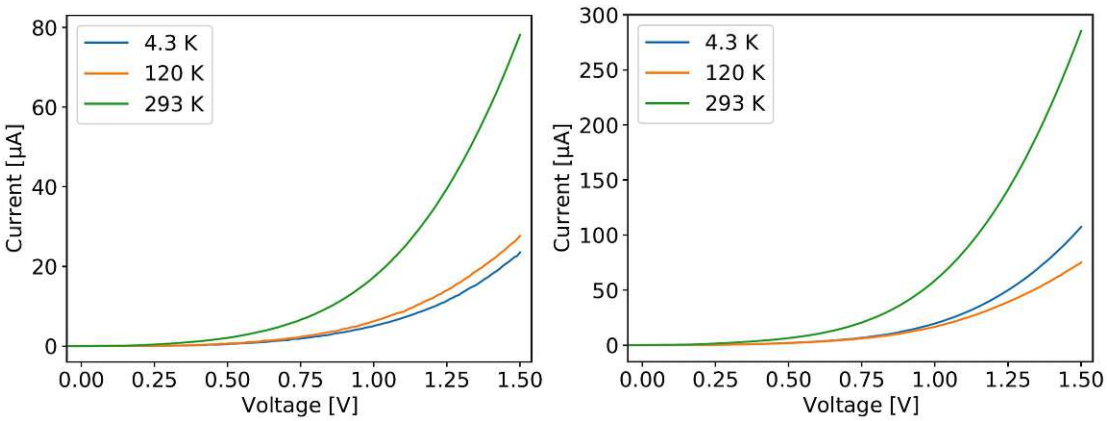

(a) 10 µm **(b)** 20 µm

Figure 4.24: Temperature dependence of the current in single 10 µm and 20 µm patch resonators. (a) The current increases with temperature for a patch size of 10 µm. (b) In contrast, for a patch size of 20 µm the current is reduced at 120 K, before it is increased at room temperature.

For the 20 µm resonators a different temperature dependent behavior than for all other patchsizes was observed, which was not expected. In L1751B compared to C1299 the temperature dependence is moderate and so is the contribution of the dark transport relative to the total current. We believe this is caused by the inherently higher conductivity of L1751B and may explain the fact that at low voltages the 2 µm current density is reduced as surface effects dominate over the dark transport, in contrast to the case of C1299. However, in both samples the estimated dark transport is of the same order, even though the interplay with present surface effects results in a different behavior.

5 Discussion and Outlook

In this work, we investigated semiconductor quantum structures with an ISB transition in the band structure that were grown by MBE. Based on these structures we used a nanofabrication process to build micro patch resonators, thereby achieving a strong light-matter coupling. By FTIR spectroscopy we measured polaritons which proved the hybridization of the electronic ISB transition and the resonant cavity mode in a doped RTD structure. Thereby, the present ISB transition was verified and the successful nanofabrication of micro patch resonators was demonstrated. Furthermore, the functionality and tunability of the resonators down to a patchsize of 1 µm was shown. We determined the patchsize resonant with the ISB transition and showed that the Rabi splitting is still present in 2 µm resonators. By low temperature IV measurements we studied the transport in single micro patch resonators down to a patchsize of 2 µm, proving the functionality of the designed contacting structure. The resonant tunneling transport in the RTD structure was shown for 20 µm patch resonators, whereas for a patchsize of 2 µm a different transport behavior was observed. In the MQW structure C1299 the collected data matches the intended tuning of a dark transport by the cavity mode volume compared to the off-resonant case of 5 µm resonators, albeit with high standard deviation. In contrast, in L1751B we measured consistent current densities for patch resonators with base areas ranging over two orders of magnitude and still observed a different transport behavior for 2 µm resonators at low voltages. Moreover, we found that surface effects influence the electronic transport, which results in a clear patch size dependence of the measured current density. However, accounting for surface effects we still observe an anomalous transport in 2 µm resonators, which we believe is caused by a dark transport. In both MQW structures the 5 µm patch resonators represented the off-resonant case and, indeed, showed the lowest current densities for voltages that are not too low, emphasizing the absence of a dark transport. Looking ahead, we believe that photocurrent measurements would be a valuable complementary experiment for gathering characteristic information about the MQW samples under investigation. A measurement of the photocurrent should confirm or refute the assumed dome-like shape in L1751, since the minimum voltage for obtaining a measurable photocurrent also depends on the form of the bandstructure. Furthermore, this would provide information about the ISB transition and the polaritonic splitting present in the respective structures. However, performing such a measurement requires a modification of the top

structure for contacting multiple patch resonators in order to enhance the total current. Additionally, an important goal in future processing runs is the improvement of the lift-off process for building the contacting structure, as this would increase the number of fabricated patch resonators, thereby leading to better statistics of the performed measurements. Further ambitions include the study of structures similar to L1751B, but with a different number of QWs, which are expected to exhibit a larger coupling strength and, thus, an enhanced dark transport, while other effects remain unchanged.

Appendix

Growth Sheet RTD C0483

Material	X	Thickness (nm)	Doping (cm^{-3})
GaAs Substrate			
GaAs		300	
AlGaAs	55	150	
Si: GaAs		70	$1 \cdot 10^{18}$
GaAs		30	
AlGaAs	40	5.1	
GaAs		10.2	
AlGaAs	40	10.2	
GaAs		10.2	
AlGaAs	40	5.1	
Si: GaAs		70	$1 \cdot 10^{18}$

Growth Sheet RTD C0484

Material	X	Thickness (nm)	Doping (cm^{-3})
GaAs Substrate			
GaAs		300	
AlGaAs	55	150	
Si: GaAs		70	$1 \cdot 10^{18}$
GaAs		30	
AlGaAs	40	5.1	
GaAs		10.2	$1 \cdot 10^{18}$
AlGaAs	40	10.2	
GaAs		10.2	$1 \cdot 10^{18}$
AlGaAs	40	5.1	
Si: GaAs		70	$1 \cdot 10^{18}$

Growth Sheet MQW C1299

Material	X	Thickness (nm)	Doping (cm^{-3})
GaAs Substrate			
GaAs		100	
AlGaAs	55	150	
Si: GaAs		60	$1 \cdot 10^{18}$
GaAs		14	
Loop 5X			
AlGaAs	19	20	
Si:GaAs		6.5	$1 \cdot 10^{17}$
End Loop			
AlGaAs	19	20	
GaAs		14	
Si: GaAs		60	$1 \cdot 10^{18}$

Growth Sheet MQW L1751B

Material	X	Thickness (nm)	Doping (cm^{-3})
GaAs Substrate			
GaAs		250	
AlGaAs	80	500	
Si: GaAs		50	$3 \cdot 10^{18}$
Loop 3X			
AlGaAs	20	20	
GaAs		0.85	
Si:GaAs		4.8	$3 \cdot 10^{17}$
GaAs		0.85	
End Loop			
AlGaAs	20	20	
Si: GaAs		50	$3 \cdot 10^{18}$

List of Figures

References

[1] E. Orgiu, J. George, J. A. Hutchison, E. Devaux, J. F. Dayen, B. Doudin, F. Stellacci, C. Genet, J. Schachenmayer, C. Genes, G. Pupillo, P. Samorì, and T. W. Ebbesen, "Conductivity in organic semiconductors hybridized with the vacuum field," *Nature Materials*, vol. 14, pp. 1123–1129, 11 2015.

[2] F. Appugliese, J. Enkner, G. L. Paravicini-Bagliani, M. Beck, C. Reichl, W. Wegscheider, G. Scalari, C. Ciuti, and J. Faist, "Breakdown of topological protection by cavity vacuum fields in the integer quantum hall effect," *Science*, vol. 375, 2022.

[3] C. Naudet-Baulieu, N. Bartolo, G. Orso, and C. Ciuti, "Dark vertical conductance of cavity-embedded semiconductor heterostructures," *New Journal of Physics*, vol. 21, 2019.

[4] G. Arwas and C. Ciuti, "Quantum electron transport controlled by cavity vacuum fields," *Physical Review B*, vol. 107, 1 2023.

[5] B. Limbacher, M. A. Kainz, S. Schoenhuber, M. Wenclawiak, C. Derntl, A. M. Andrews, H. Detz, G. Strasser, A. Schwaighofer, B. Lendl, J. Darmo, and K. Unterrainer, "Resonant tunneling diodes strongly coupled to the cavity field," *Applied Physics Letters*, vol. 116, p. 221101, 6 2020.

[6] G. Plunien, B. Muller, and W. Greiner, "The casimir effect," 1986.

[7] R. Loudon, *The Quantum Theory of Light Third Edition*. 2000.

[8] E. M. Purcell, "Spontaneous emission probabilities at radio frequencies," *Physical Review*, vol. 69, p. 681, 1946.

[9] H. Walther, B. T. Varcoe, B. G. Englert, and T. Becker, "Cavity quantum electrodynamics," *Reports on Progress in Physics*, vol. 69, pp. 1325–1382, 4 2006.

[10] G. T. Moore, "Quantum theory of the electromagnetic field in a variable-length one-dimensional cavity," *Journal of Mathematical Physics*, vol. 11, pp. 2679–2691, 1970.

[11] C. M. Wilson, G. Johansson, A. Pourkabirian, M. Simoen, J. R. Johansson, T. Duty, F. Nori, and P. Delsing, "Observation of the dynamical casimir effect in a superconducting circuit," *Nature*, vol. 479, pp. 376–379, 11 2011.

[12] S. Vezzoli, A. Mussot, N. Westerberg, A. Kudlinski, H. D. Saleh, A. Prain, F. Biancalana, E. Lantz, and D. Faccio, "Optical analogue of the dynamical casimir effect in a dispersion-oscillating fibre," *Communications Physics*, vol. 2, 12 2019.

[13] P. Forn-Díaz, L. Lamata, E. Rico, J. Kono, and E. Solano, "Ultrastrong coupling regimes of light-matter interaction," *Reviews of Modern Physics*, vol. 91, 6 2019.

[14] P. B. Vigneron, S. Pirotta, I. Carusotto, N. L. Tran, G. Biasiol, J. M. Manceau, A. Bousseksou, and R. Colombelli, "Quantum well infrared photo-detectors operating in the strong light-matter coupling regime," *Applied Physics Letters*, vol. 114, 4 2019.

[15] Demtröder, *Experimentalphysik 3, Atome, Moleküle, Festkörper*, vol. 3. 2010.

[16] P. Rabl, *Theoretical Quantum Optics*. 2016.

[17] C. Ciuti, G. Bastard, and I. Carusotto, "Quantum vacuum properties of the intersubband cavity polariton field," *Physical Review B - Condensed Matter and Materials Physics*, vol. 72, p. 115303, 9 2005.

[18] S. Adachi, *GaAs and Related Materials*. WORLD SCIENTIFIC, 1994.

[19] M. U. Khan, M. S. Sharawi, and R. Mittra, "Microstrip patch antenna miniaturisation techniques: A review," 6 2015.

[20] S. Büttgenbach, *Mikrosystemtechnik*. Springer Berlin Heidelberg, 2016.

[21] C. Bryce and D. Berk, "Kinetics of GaAs dissolution in H_2O_2-NH_4OH-H_2O solutions," 1996.

[22] S. Golka, S. Schartner, W. Schrenk, and G. Strasser, "Low bias reactive ion etching of GaAs with a $SiCl_4/N_2/O_2$ time-multiplexed process," *Journal of Vacuum Science Technology B: Microelectronics and Nanometer Structures Processing, Measurement, and Phenomena*, vol. 25, pp. 839–844, 5 2007.

[23] P. Norton, "HgCdTe infrared detectors," 2002.